



**HAL**  
open science

## Stratigraphic architecture and fault offsets of alluvial terraces at Te Marua, Wellington fault, New Zealand, revealed by pseudo-3D GPR investigation,

S. Beaupretre, I. Manighetti, S. Garambois, J. Malavieille, S. Dominguez

### ► To cite this version:

S. Beaupretre, I. Manighetti, S. Garambois, J. Malavieille, S. Dominguez. Stratigraphic architecture and fault offsets of alluvial terraces at Te Marua, Wellington fault, New Zealand, revealed by pseudo-3D GPR investigation,. *Journal of Geophysical Research: Solid Earth*, 2013, 118 (8), pp.4564-4585. 10.1002/jgrb.50317 . hal-00873350

**HAL Id: hal-00873350**

**<https://hal.science/hal-00873350>**

Submitted on 11 May 2021

**HAL** is a multi-disciplinary open access archive for the deposit and dissemination of scientific research documents, whether they are published or not. The documents may come from teaching and research institutions in France or abroad, or from public or private research centers.

L'archive ouverte pluridisciplinaire **HAL**, est destinée au dépôt et à la diffusion de documents scientifiques de niveau recherche, publiés ou non, émanant des établissements d'enseignement et de recherche français ou étrangers, des laboratoires publics ou privés.

# Stratigraphic architecture and fault offsets of alluvial terraces at Te Marua, Wellington fault, New Zealand, revealed by pseudo-3D GPR investigation

S. Beauprêtre,<sup>1</sup> I. Manighetti,<sup>1,2</sup> S. Garambois,<sup>1</sup> J. Malavieille,<sup>3</sup> and S. Dominguez<sup>3</sup>

Received 7 May 2013; revised 26 July 2013; accepted 29 July 2013; published 22 August 2013.

[1] Past earthquake slips on faults are commonly determined by measuring morphological offsets at current ground surface. Because those offsets might not always be well preserved, we examine whether the first 10 m below ground surface contains relevant information to complement them. We focus on the Te Marua site, New Zealand, where 11 alluvial terraces have been dextrally offset by the Wellington fault. We investigated the site using pseudo-3D Ground Penetrating Radar and also produced a high-resolution digital elevation model (DEM) of the zone to constrain the surface slip record. The GPR data reveal additional information: (1) they image the 3D stratigraphic architecture of the seven youngest terraces and show that they are strath terraces carved into graywacke bedrock. Each strath surface is overlain by 3–5 m of horizontally bedded gravel sheets, including two pronounced and traceable reflectors; (2) thanks to the multilayer architecture, terrace risers and channels are imaged at three depths and their lateral offsets can be measured three to four times, constraining respective offsets and their uncertainties more reliably; and (3) the offsets are better preserved in the subsurface than at the ground surface, likely due to subsequent erosion-deposition on the latter. From surface and subsurface data, we infer that Te Marua has recorded six cumulative offsets of 2.9, 7.6, 18, 23.2, 26, and 31 m ( $\pm 1$ –2 m). Large earthquakes on southern Wellington fault might produce 3–5 m of slip, slightly less than previously proposed. Pseudo-3D GPR thus provides a novel paleoseismological tool to complement and refine surface investigations.

**Citation:** Beauprêtre, S., I. Manighetti, S. Garambois, J. Malavieille, and S. Dominguez (2013), Stratigraphic architecture and fault offsets of alluvial terraces at Te Marua, Wellington fault, New Zealand, revealed by pseudo-3D GPR investigation, *J. Geophys. Res. Solid Earth*, 118, 4564–4585, doi:10.1002/jgrb.50317.

## 1. Introduction

[2] Even in regions where earthquake activity is intensively monitored and where a large number of multidisciplinary studies are conducted to assess seismic hazard, we may fail to properly anticipate the maximum magnitude of the forthcoming events (e.g., 2011 Tohoku earthquake) [e.g., Ozawa *et al.*, 2011]. To tighten the magnitude estimates for a given fault, a precise knowledge of the slips produced by the large prehistorical earthquakes on the fault is mandatory. Yet this information is extremely difficult to obtain because it mainly

resides in more or less preserved imprints that previous large earthquakes produced in the surface morphology [e.g., Burbank and Anderson, 2001]. Many studies have thus been conducted over the last decades to search for this morphological information [e.g., McCalpin, 2009]. The objective is to identify preserved morphological markers (such as river beds, alluvial terraces, moraine spurs, alluvial fans, coral constructions, etc.) on the ground surface that would be offset or deformed by the fault. As most of the surface offsets are the result of repeated coseismic fault slips over time, their systematic measurement for markers of different ages allows building slip histories, sometimes down to the earthquake scale [e.g., Gaudemer *et al.*, 1995; Tapponnier *et al.*, 2001; Liu *et al.*, 2004; Zielke *et al.*, 2010; Klinger *et al.*, 2011]. Yet, one strong hypothesis underlying such an approach is that the original shape of the offset markers has not significantly or systematically been modified since their time of formation, that the markers truly behave as passive features, and that the fault offset that they have recorded reflects the actual slip on the fault. Though reasonable, these hypotheses face the fact that the ground surface is exposed to dynamic processes—weathering, erosion, deposition, human activities, etc., that all contribute to modify its morphology over time. We have no means to evaluate these possible modifications. Therefore, to overcome this

Additional supporting information may be found in the online version of this article.

<sup>1</sup>Institut des Sciences de la Terre, Université Joseph Fourier and CNRS (UMR 5275), Maison des Géosciences, Saint Martin d'Hères, France.

<sup>2</sup>Géoazur, Université de Nice Sophia Antipolis, CNRS, IRD, Observatoire de la Côte d'Azur, Sophia Antipolis, France.

<sup>3</sup>Laboratoire Géosciences Montpellier, CNRS (UMR5243), Université de Montpellier 2, Montpellier, France.

Corresponding author: I. Manighetti, Géoazur, Université de Nice Sophia Antipolis, CNRS, IRD, Observatoire de la Côte d'Azur, 250 rue Albert Einstein, Sophia Antipolis, 06560 Valbonne, France. (manighetti@geoazur.unice.fr)

©2013. American Geophysical Union. All Rights Reserved.  
2169-9313/13/10.1002/jgrb.50317

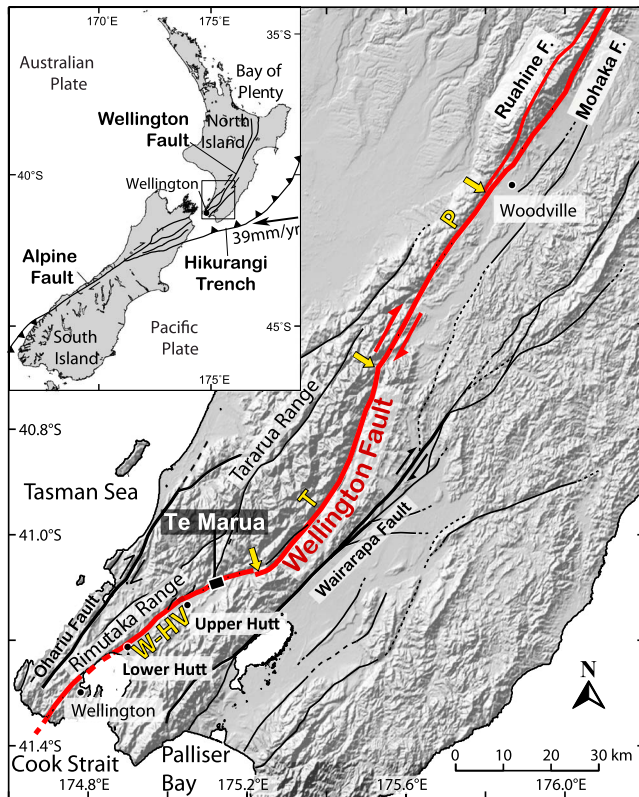


**Figure 1.** Tectonic setting of southern North Island, New Zealand, and location of Te Marua site. Only major active faults are represented (black traces), with the Wellington Fault in red. The black box indicates the location of Te Marua site. The major Wellington fault segments are denoted with letters (W-HV: Wellington-Hutt Valley segment; T: Tararua segment; P: Pahiatua segment) and are separated by yellow arrows that mark the major intersegment zones. Inset shows the Australian-Pacific plate setting in New Zealand, with the box indicating the figure.

problem, one common approach is to focus on the youngest offsets as those are expected to be the best preserved as well as the most abundant in the ground morphology.

[3] We approach this question differently. In an earlier paper [Beaupretre et al., 2012], we suggested, as others before [e.g., McCaillin, 2009], that part of the past earthquake offsets might be buried in the first few meters below the current ground surface. Yet, to investigate this hypothesis, we developed a novel paleoseismological approach, based on a specific use of pseudo-3D ground penetrating radar (GPR) surveying. Although it has become fairly common that 2D-, pseudo-3D, and 3D GPR are used to investigate the shallow geometry of fault planes and fault zones (mainly fault-perpendicular GPR profiles) [e.g., Gross et al., 2000, 2002, 2003, 2004, Troncke et al., 2004; McClymont et al., 2008a, 2008b, 2010; Carpentier et al., 2012], our earlier work [Beaupretre et al., 2012] is the first attempt to use pseudo-3D GPR to reveal buried fault-offset markers on either side of the fault (parallel-fault GPR profiles). We tested this original approach at one site of the seismogenic strike-slip Hope fault, New Zealand, and showed that we could successfully image a large number of dextrally displaced, abandoned, buried stream channels, whose lateral offsets could be precisely measured.

This work thus suggested that pseudo-3D GPR can be used to reveal and measure past fault slips in the shallow subsurface and hence to provide new data complementary to surface measurements, especially where surface features are few.

[4] In the present study, we examine a specific case where a number of fault offsets have already been measured in the current morphology and question whether the deep subsurface ( $> \sim 2$  m, i.e., deeper than the shallow subsurface documented by trenching studies) contains additional information that might be useful to further document the earthquake slips on the fault. We address this question at a site—Te Marua (Figure 1) located on the major seismogenic dextral Wellington fault, New Zealand. The site shows 11 well-preserved alluvial terraces that are dextrally displaced by the Wellington fault. The lateral offsets of the terraces have been extensively studied in previous morphological and paleoseismological analyses [e.g., Lensen, 1958; Berryman, 1990; Van Dissen et al., 1992; Little et al., 2010; Langridge et al., 2011], so that most of the ground surface information has already been recovered.

[5] We investigated the Te Marua site using dense, pseudo-3D, multifrequency GPR acquisitions. More precisely, we acquired forty,  $\sim 600$  m long GPR profiles parallel to and evenly distributed either side of the fault trace, and spaced by  $\sim 5$  m. The total area covered is about  $600 \text{ m} \times 200 \text{ m}$ . We also produced a high-resolution GPS-RTK digital elevation model (DEM) of the site spanning a slightly larger area of  $600 \text{ m} \times 300 \text{ m}$ . The GPS-derived DEM allows us to examine the Te Marua morphology in great detail, while the GPR data image the architecture of the subsurface at high resolution, down to 5–7 m depth. Taken together, the data allow us to measure the lateral fault offsets preserved in both the subsurface and at the surface, and to examine whether those are similar or not. The GPR data also document the stratigraphic architecture of the seven most recent alluvial terraces, which was unknown up to now.

## 2. Alluvial Setting and Slip Record at Te Marua, Wellington Fault

### 2.1. The Wellington Fault

[6] In the southern North Island of New Zealand, the Pacific and Australian plates converge in an oblique fashion (Figure 1). Their relative motion is partitioned into  $\sim 34$  mm/yr of shortening and  $\sim 26$  mm/yr of lateral motion [Barnes et al., 1998; Nicol et al., 2007]. Most of the shortening is accommodated by thrust faulting and folding nearby the Hikurangi Trench, 150 km east of Wellington city. The majority of the lateral motion is accommodated on several right lateral strike-slip faults, including the Ohariu-, Wellington-, and Wairarapa fault (Figure 1) [Barnes et al., 1998; Nicol et al., 2007].

[7] The Wellington dextral fault poses an elevated seismic risk in New Zealand since it passes directly through the Wellington city. It strikes  $N40^\circ E$  and extends between offshore Cook Strait [Pondard and Barnes, 2010] and Woodville. From there, it splays into the Mohaka and Rauhine faults, which extend up to the Bay of Plenty (Figure 1) [Langridge et al., 2005; Mouslopoulou et al., 2007]. The fault is thought to have accumulated at least 8 km of lateral slip over the last  $\sim 2$  Myr [Begg and Mazengarb, 1996; Beanland and Haines, 1998; Nicol et al., 2007], although it may have a longer slip history. Along the Cook Strait-to-Woodville strand ( $\sim 170$  km long), the fault is divided into three major segments separated by large

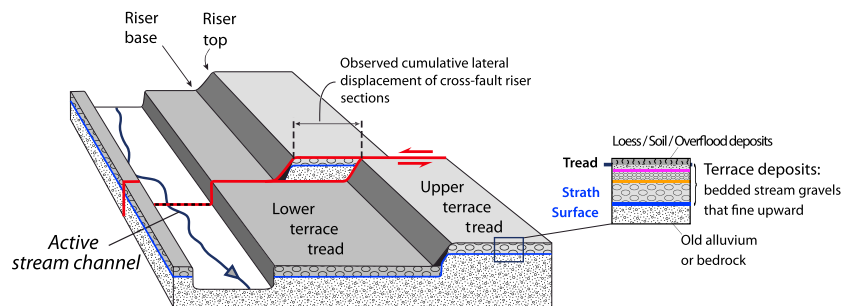


**Figure 2.** Block diagram presenting the common vision of the architecture of alluvial terraces laterally offset by a strike-slip fault [modified from *Gold et al.*, 2011]. The inset shows details on the gravel pile, with colors coinciding with the stratigraphic horizons detected in the GPR data (compare with Figures 8 and 9).

bends and step overs (Figure 1) [Berryman *et al.*, 2002; Langridge *et al.*, 2005, 2007]. The Te Marua site is located in the southernmost of these segments, the ~75 km long Wellington-Hutt Valley segment (WHV), which is thought to represent an individual rupture segment [Berryman, 1990; Langridge *et al.*, 2005]. The Quaternary slip rate on the WHV fault segment is estimated at 5.1–8.2 mm/yr [Berryman, 1990; Grapes, 1993; Berryman *et al.*, 2002; Langridge *et al.*, 2005; Little *et al.*, 2010; Ninis *et al.*, 2013].

[8] No major historical earthquake has been reported on the Wellington-Hutt Valley segment since the European settlement in ~1840 AD. Paleoseismological studies suggest that at least five major earthquakes broke the WHV segment in the last ~9 ka; at  $210 \pm 100$  yr, 790–895 yr, 1830–2340 yr, 2460–4500 yr, and 7290–8380 yr B.P. [Van Dissen *et al.*, 1992; Van Dissen and Berryman, 1996; Langridge *et al.*, 2009, 2011; Little *et al.*, 2010; Ninis *et al.*, 2013], while five more events might have occurred between 7300 and 11,600 yr B.P. [Langridge *et al.*, 2009]. The offsets of these paleo-earthquakes along the WHV segment are estimated in the range 4.2–5.0 m [Berryman, 1990; Little *et al.*, 2010], while the magnitudes are inferred to be Mw 7.3–7.9 [Berryman, 1990; Van Dissen and Berryman, 1996; Little *et al.*, 2010].

## 2.2. Alluvial Setting and Terraces at Te Marua

[9] In the Hutt Valley, the Wellington fault extends at the base of the Rimutaka Range (Figure 1), where a series of alluvial terraces have been emplaced over the Quaternary. Some of these terraces stand at high relative elevation above the present river beds and are fill aggradation terraces that were formed during stadial episodes [Berryman, 1990; Grapes, 1993; Ninis *et al.*, 2013]. In the Te Marua area, the youngest fill terrace has been dated at 12–13 kyr, coincident with the approximate age of the Last Glacial Maximum in the North Island [Berryman, 1990; Grapes, 1993; Little *et al.*, 2010; Ninis *et al.*, 2013].

[10] Since this last aggradation period, downcutting occurred and fluvial degradation terraces have formed. A degradation terrace forms by lateral stream erosion into preexisting alluvium (so-called “fill-cut” terrace) or bedrock (so-called “strath” terrace) during periods of static equilibrium that are followed by renewed stream-channel downcutting that isolates the terrace surface. Fill-cut and strath terraces are thus genetically the same [Bull, 1990]; therefore, the term “strath” is broadly used to describe the erosional base of a terrace [Bucher, 1932], while the term “tread” describes the terrace

surface [Campbell, 1929], and the term “riser” describes the erosional escarpment that separates two terrace treads of different age and elevation (Figure 2) [e.g., Cowgills, 2007]. The strath of a terrace is the paleo-valley bottom base, while the terrace tread is the constructional top of the paleo-flood plain. The deposits between the strath and tread are thus basically stream gravels that are genetically related to the strath carving (Figure 2) [Gilbert, 1877; Mackin, 1937; Bull, 1990; Hancock and Anderson, 2002; Wegmann and Pazzaglia, 2002]. These gravels are commonly several meters thick, are well-sorted and fine upward, ranging from coarse gravel immediately above the erosional strath surface to fine-grained (clay, silt, and fine sand) deposits near the terrace tread (Figure 2) [e.g., Bull, 1990; Merritts and Hesterberg, 1994; Pazzaglia, 2013].

[11] At Te Marua, the Wellington fault cuts across a flight of 11 Holocene degradation terraces that formed below the level of the most recent 12–13 ka Ohakea aggradation terrace (named T12), in a meander of the Hutt River (Figure 3) [Lensen, 1958; Berryman, 1990; Van Dissen *et al.*, 1992; Little *et al.*, 2010; Ninis *et al.*, 2013]. These degradation terraces have been labeled T1 through T11, with T1 representing the lowest (~3 m above present river bed) and hence youngest terrace tread above the modern river bed, while the successively larger numbers represent the progressively higher and hence older terrace surfaces (Figure 3) [Lensen, 1958; Berryman, 1990; Van Dissen *et al.*, 1992; Little *et al.*, 2010]. The stratigraphic architecture of the terraces is unknown, whereas it is not clear whether the youngest T1–T8 terraces are fill-cut or strath. The common interpretation is that they are fill-cut terraces that were carved into the T12 fill alluvium deposits (see Figure S1 in the supporting information) [Berryman, 1990; Little *et al.*, 2010; Ninis *et al.*, 2013] but evidence are lacking to validate this interpretation. The only outcrop at Te Marua is the modern river bank, and there, gravels are observed to overlie the graywacke bedrock that stands at 3 m below the current ground surface [Little *et al.*, 2010]. A few trenches have been excavated at Te Marua, but they do not go deeper than 1.5–2 m and only show a variety of gravels, sands, and silts [Langridge *et al.*, 2011]. At one site ~2 km from Te Marua, a 6–10 m high cut adjacent to the Te Marua water reservoir shows a multilayer sequence of gravels several meters thick overlying the graywacke bedrock (Figure 4) [Berryman, 1990]. The 3D GPR images that were acquired on a small area (50 × 50 m) in the T6 Te Marua terrace (precise location not provided in the source paper) suggest that the graywacke

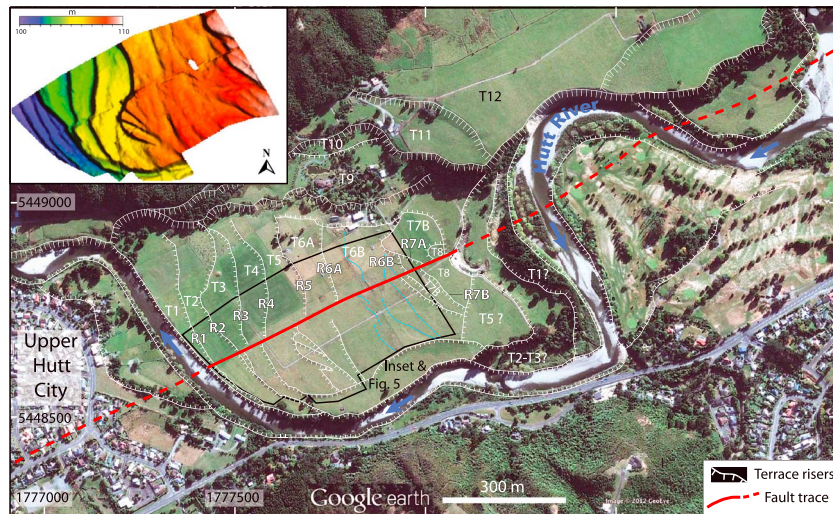


**Figure 3.** Google Earth view of the Te Marua site, showing the Hutt River, the Wellington fault trace (in red), and the various terraces, whose risers are underlined in white. Riser and terrace names are indicated (degradation terraces in white, and fill terraces in black). Major abandoned stream channels are in blue. The black box indicates the zone covered with our GPS-derived DEM shown in inset and in Figure 5.

bedrock extends at a remarkably constant depth of  $4.5 \pm 0.6$  m, below flat-lying alluvial gravel sheets [Gross *et al.*, 2004]. The 3D GPR images ( $50 \times 25$  m) that were acquired in the nearby Totara Park ( $< 3$  km away) reveal 3–6 m thick, flat-lying gravel sheets above the graywacke bedrock that stands at 4–5 m depth [Gross *et al.*, 2004; McClymont *et al.*, 2008b]. These various observations thus suggest that the graywacke bedrock lies at a relatively shallow depth beneath the Te Marua degradation terraces, while at least some of those terraces are made of flat-lying gravel sheets a few meters thick. Therefore, the Te Marua terraces might be strath terraces, with an architecture and stratigraphy similar to those sketched in Figure 2. If that is the case, we expect GPR data to reveal a number of subhorizontal horizons.

### 2.3. Slip Record at Te Marua

[12] At the Te Marua site the Wellington fault has progressively offset the degradational terraces T1–T8, the corresponding risers, as well as a number of channels which incised into these terraces.

[13] Using field measurements made by tape, Berryman [1990] estimated the most recent coseismic slip at 3.7–4.7 m (Table 1). He found no offset of the youngest terrace T1 or its upper riser R1. More recently, Little *et al.* [2010] analyzed GPS-derived topographic maps of Te Marua and estimated the last event displacement to be  $5.3 \pm 0.8$  m, which also does not offset T1 or R1. Little *et al.* [2010] measured a total of 12 lateral offsets across the various terraces and channels, and found these offsets to cluster around three mean values,  $5.3 \pm 0.8$  m (four offset measurements),  $14.3 \pm 3.1$  m (two offset measurements), and  $20.1 \pm 1.2$  m (six offset measurements). They inferred that four large, fairly characteristic earthquakes, each with a mean slip of  $5.0 \pm 0.2$  m, produced the measured offsets. This inference thus assumes that the penultimate of these four events is not represented in the geomorphic record. Age constraints on these earthquakes are provided by Van Dissen *et al.* [1992], Little *et al.* [2010], and Langridge *et al.* [2011].

Taken together they suggest that the most recent event occurred after 250 cal yr B.P., the terraces T1–T6 were formed and abandoned in the last  $4.5 \pm 0.4$  ka, and the oldest T12 fill terrace was abandoned about 12–13 ka ago.

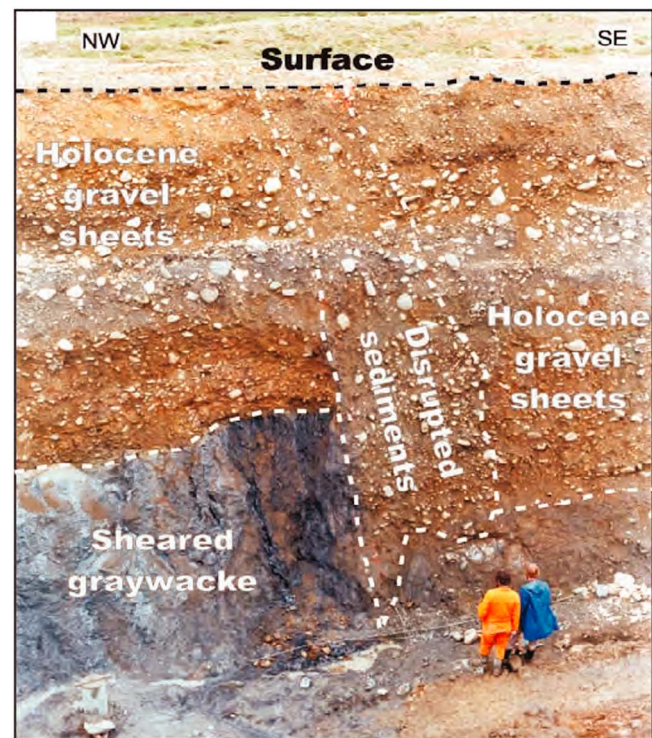


**Figure 4.** Picture of the Wellington Fault exposed in an 8–10 m deep cut excavated for a water reservoir, a few km away from Te Marua [from Gross *et al.*, 2004; Berryman, 1990, and reference therein]. A pile of multilayered gravel sheets overlay the graywacke bedrock.

**Table 1.** Comparison of the Different Sets of Offset Measurements Performed at the Ground Surface at Te Marua [This Study; *Little et al.*, 2010; *Berryman*, 1990; *Lensen*, 1958]<sup>a</sup>

This Study, At Surface			<i>Little et al.</i> , 2010			<i>Berryman</i> , 1990			<i>Lensen</i> , 1958	
Landform	Dextral Offset (m)	Error (m)	Landform	Dextral Offset (m)	Error (m)	Landform	Dextral Offset (m)	Error (m)	Landform	Dextral Offset (m)
<b>R1</b>	1.6	1.0	<b>R1</b>	0	NA	Riser <b>R1</b>	0	NA	-	-
T2-Ch1_W	6.4	1.1	Channel 1	5.4	1.7	Channel (022)	3.7	0.3	-	-
T2-Ch1_E	6.1	0.8	Channel interfluve	4.3	1.5	-	-	-	-	-
T2-Ch2_W	7.6	0.9	Channel 2	5.4	1.8	Channel (023)	4.7	0.3	-	-
T2-Ch2_E	6.1	0.6								
<b>R2</b>	5.3	0.8	<b>R2</b>	5.5	0.8	<b>R2</b> (024)	7.4	NA	Terrace III–IV	5.5 (18 ft)
<b>R3</b>	17.9	1.1	<b>R3</b>	14.4	0.5	<b>R3</b> (025)	18	NA	Terrace II–III	15.2 (50 ft)
T4-Inc1	15.8	5.0	-	-	-	-	-	-	-	-
T4-Inc2	17.5	1.6	-	-	-	-	-	-	-	-
<b>R4</b>	16.5	1.3	<b>R4</b>	13.1	2.6	<b>R4</b> (026)	19	NA	Terrace I–II	15.2 (50 ft)
T5-Ch1_W	-	-	-	-	-	-	-	-	-	-
T5-Ch1_E	18.4	1.7	-	-	-	-	-	-	-	-
T5-Ch2	15.1	1.9	-	-	-	-	-	-	-	-
<b>R5</b>	21.1	1.4	<b>R5</b>	20.8	0.8	Riser (028)	42	NA	-	-
T6a-Ch1	22.1	1.8	-	-	-	-	-	-	-	-
T6a-Ch2_W	18.8	1.6	-	-	-	-	-	-	-	-
T6a-Ch2_E	19.3	1.6	-	-	-	-	-	-	-	-
T6a-Ch3	22.3	1.2	-	-	-	-	-	-	-	-
<b>R6A</b>	26.3	1.5	Channel 3	18.9	5.4	-	-	-	-	-
T6b-Inc1	26.2	1.7	-	-	-	-	-	-	-	-
T6b-Ch1	25.5	2.3	-	-	-	-	-	-	-	-
T6b-CH1	25.0	3.2	Channel 4	17.4	4.2	-	-	-	-	-
T6b-Ch2	25.0	10.0	-	-	-	-	-	-	-	-
T6b-CH2	25.7	3.0	-	-	-	-	-	-	-	-
T6b-CH3	24.4	1.3	-	-	-	-	-	-	-	-
<b>R6B</b>	31.4	1.8	<b>R6</b>	18.6	1.6	Riser (033)	20	NA	-	-
<b>R7A</b>	37.0	3.1	Channel 5	18.6	2.6	-	-	-	-	-

<sup>a</sup>Offsets from present study come from Table S1 in supporting information. Principal risers are highlighted in gray.

### 3. Data Acquisition and Processing

#### 3.1. Surface Data

[14] We used two real-time kinematic GPS systems (RTK) to precisely locate the GPR profiles and map the landforms at Te Marua over an area of 600 m × 300 m around the fault trace (Figure 5). Kinematic GPS-surveying provides survey measurements with a precision of ~3 cm horizontally and ~20 cm vertically. Over the five days of acquisition, we surveyed a total of 74,680 points with a sampling frequency of 1 Hz, providing a spatial sampling of the topography of ~0.41 pt.m<sup>-2</sup> (see supporting information Figure S2 that shows location of GPS data). The data were spatially filtered to remove duplicate points and interpolated onto a 2 m × 2 m grid (Figure 5). The obtained DEM images at high resolution the landforms that shape the Te Marua site; basically a flight of alluvial terraces that increase in elevation from west to east, in a step fashion across steep risers (Figure 5).

#### 3.2. GPR Data Acquisition and Processing

[15] Among the available geophysical methods for subsurface imaging, GPR is the most appropriate, combining high speed acquisition with high resolution down to depths of ~1–10 m. It records travel times and amplitudes of reflected and scattered electromagnetic waves, generated by contrasts in the electromagnetic properties of the deposits (dielectric permittivity, electrical resistivity, and magnetic permeability). Even minor changes in porosity, water content, grain type or

grain shape, orientation, and packing generate sufficiently distinct reflections in GPR records whose continuity can be imaged [e.g., *Neal*, 2004; *Annan*, 2009]. For these reasons, GPR is nowadays increasingly used for various geological issues, including fault and stratigraphic studies, both in 2D and, more recently, in 3D [e.g., *McClymont et al.*, 2008a]. However, a full 3D imaging requires a GPR acquisition with at least a quarter wavelength spacing grid in all directions on the surveyed area [*Grasmueck et al.*, 2005]. This means that, in an example case of sedimentary deposits through which the electromagnetic waves would have a typical mean velocity of 12 cm/ns, a full 3D GPR investigation would require the acquisition of survey profiles spaced by at most 30 cm in all directions (with a 100 MHz antenna; to be compared with the ~5 m spacing that we used). Such an extremely dense acquisition necessarily restricts 3D applications to small areas. Fortunately, in cases where the investigated subsurface features are expected to be fairly linear and of homogeneous orientation (2D media), anisotropic acquisition with dense GPR-trace collection in the direction perpendicular to the expected 2D features and sparser trace collection in the other direction may be an appropriate approach [*Beaupretre et al.*, 2012]. Such a pseudo-3D GPR approach is thus well-suited investigating piercing lines oriented perpendicular to a fault trace, as might be produced by stream channels and terrace risers. Furthermore, the pseudo-3D approach allows to investigate relatively large areas (several 1000 m<sup>2</sup>), thereby allowing to capture large lateral offsets.

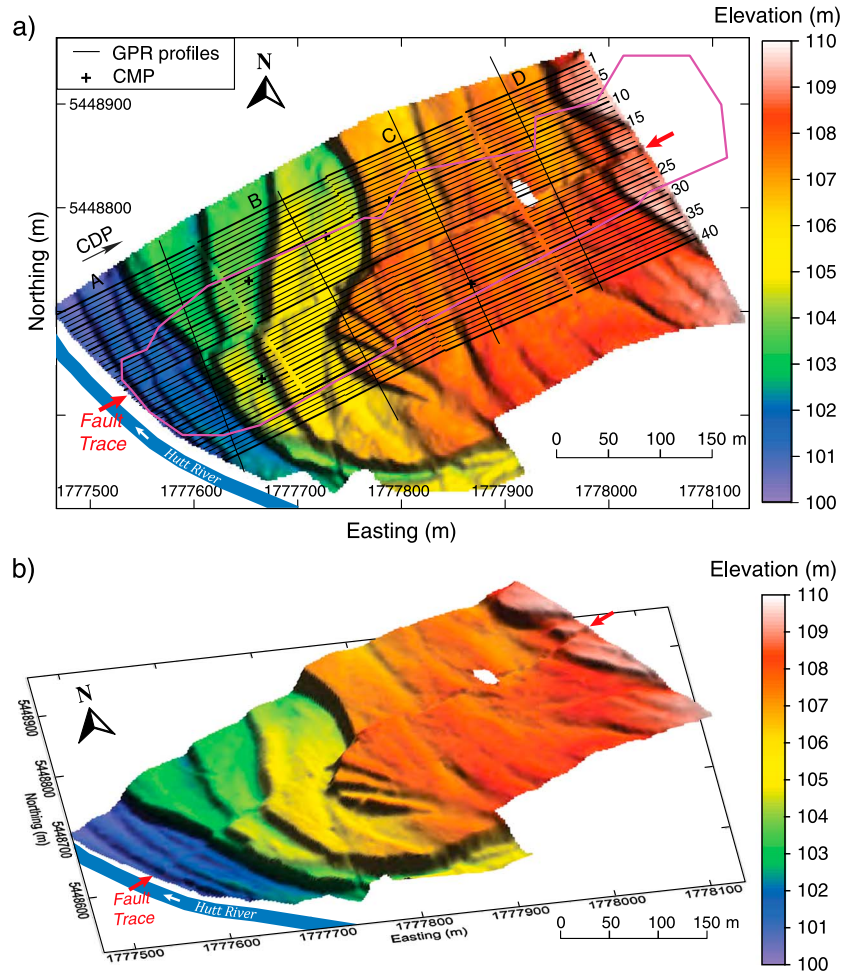


**Figure 5.** (a) Location of GPR profiles and CMPs on the GPS-derived DEM, illuminated from the NE. Red arrows indicate the fault trace. The GPR fault-parallel profiles are numbered 1 to 40 from north to south, and each is divided into four subsections A, B, C, D (limited by fences). GPR images are presented in Figure S4. Coordinates are in NZTM 2000 reference frame. The purple rectangle locates the DEM previously produced by *Little et al.* [2010]. (b) Three-dimensional perspective image of the DEM, which best shows the step arrangement of the terraces that increase in elevation from west to east, away from the present Hutt riverbed.

[16] In this study, we acquired forty,  $\sim 600$  m long GPR profiles parallel to and evenly distributed (with a  $\sim 5$  m spacing) on either side of the fault trace (Figure 5). Overall, the investigated area is  $\sim 600$  m  $\times$  200 m large. In order to avoid the perturbations of the subsurface architecture expected in the immediate vicinity of the fault trace, we did not acquire any GPR data in a  $\sim 10$  m wide zone roughly centered on the fault trace (Figure 5). The profiles were acquired with a RAMAC multichannel GPR system (MALÅ Geosciences) connected to two antennas, a 250 MHz shielded antenna (transmitter-receiver distance of 0.36 m), and a 100 MHz unshielded antenna specifically designed for rough terrains (transmitter-receiver distance of 2 m). The use of two antennas allowed us to obtain complementary GPR images, with different vertical resolutions and penetration depths. On each profile, the system was triggered every 20 cm thanks to a hip chain or a calibrated encoding wheel. The 250 MHz data were acquired with a sampling frequency of 2481 MHz on a 271 ns recording time window, while the 100 MHz data were acquired with a sampling frequency of 1152 MHz on

a 419 ns time window. In addition, six Common Mid-Point surveys were measured at different locations of the site to quantify the electromagnetic wave velocity variability [e.g., *Garambois et al.*, 2002]. The equipment and site environment are shown in supporting information Figure S3, while the individual GPR images are presented in Figure S4.

[17] We processed each profile following the classical processing flow sequence for 2D GPR data described by *Cassidy* [2009]. Each profile was first preprocessed, regardless of sampling frequency, to correct for time zero drifts; this is done by matching the direct air-wave with the actual arrival time. The GPR data were then interpolated to a 20 cm sampling rate (rubber-banding process) to ensure a constant intertrace spacing. To properly tie the GPR acquisitions to the GPS positioning, we measured common GPS-GPR points every  $\sim 50$  m along the profiles, and the positions of the GPR profile extremities. The GPR profiles were then filtered using an adapted “dewow” zero-phase low-cut filter made to remove the continuous component or low frequency bias in the data [Fisher et al., 1994]. Signal reverberation that

occurs when GPR signal repeatedly bounces within an antenna or between two antennae [Annan, 2005] produces antenna-ringing effects that may obliterate the signals of interest in attenuating materials (e.g., low resistive soils). To attenuate these undesirable signals, we computed a mean trace for each profile, which we then subtracted from each trace. This process, referred to as “background removal,” also suppresses the direct waves and thus enhances the visualization of the late depth-reflected arrivals [e.g., Cassidy, 2009]. Data were then normalized trace by trace and filtered by a weighted running average filter that had been computed every three traces to enhance the continuity of any flat-lying or low-dipping interfaces. All these classical processes were performed using the Seismic Unix software [Cohen and Stockwell, 1999].

[18] We then applied to all GPR data (1) static corrections made to remove the effects of topography, (2) dynamic corrections computed to simulate zero-offset data (normal incidence), and (3) conversions of two-way propagation time to depth [e.g., Cassidy, 2009]. To perform these three corrections, the knowledge of the 3D electromagnetic velocity field in the medium is required. To approach it, we acquired six Common Mid-Point surveys in different areas of the site (Figure 5), by progressively increasing the distance (20 cm steps) of the 100 MHz and 200 MHz antennas to a central location [e.g., Deparis and Garambois, 2009]. The normal moveout (NMO) of the main reflected events was then analyzed by a combined approach where a semblance maxima analysis that yields the stacking velocity is refined using a hyperbola fitting [Garambois et al., 2002]. The results show a vertical and lateral variability of the NMO velocities that ranges from  $\sim 10.3$  to  $14.0$  cm/ns. These variations may reflect changes in the sediment grain size and arrangement, and/or variations in water content, or may also result from the presence of nonplanar reflectors in the medium. As we have no means to discriminate these factors in such a large area, our only option is to use an average velocity that smooths out the local variations and aims to well represent the entire medium [e.g., McClymont et al., 2008b]. From the various NMO velocities we obtained, we infer that a mean velocity of  $12$  cm/ns ( $\pm 2$ ) is reasonable. We thus use this mean velocity in all data processing steps where knowledge of the velocity field is required.

### 3.3. Extracting the Stronger Reflections in the GPR Data

[19] Even small changes in dielectric permittivity at either physical boundaries (i.e., water table, fracture and fault plane, depositional and stratigraphic contact, large vegetation roots, etc.) or zones where the material properties are being changed can produce reflections in GPR data [e.g., Bristow and Jol, 2003]. If these reflections are strong and continuous, it is likely that they represent physical boundaries or property changes which are significant and/or over large extents. As summarized in section 2.2, previous studies at Te Marua suggest that at least some of the Te Marua terraces are made of sequences of flat-lying gravel sheets a few meters thick, as shown in Figures 2 and 4. We thus expect that the GPR data might reveal several quite strong and continuous reflections within each of the alluvial degradation Te Marua terraces.

[20] To search for these possible reflections in the GPR data, we first tested different gains for data display (exponential

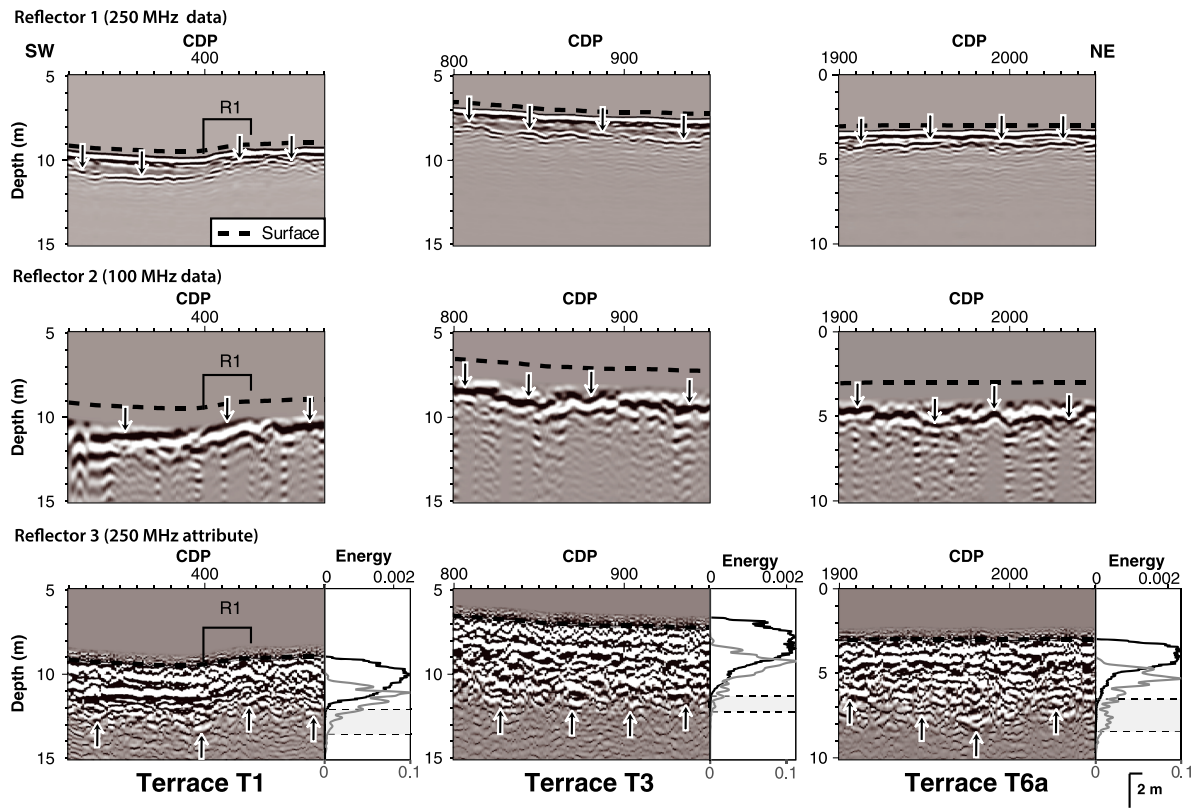
gain, dynamic automatic gain control) [Cassidy, 2009], settling on the gain which most clearly highlights internal reflections. We then carefully scrutinized the enhanced data within each terrace, to search for any clear reflector that would be continuous at least from one zone of a terrace to another and from one profile to the next across a terrace. In doing so, we recognized, within each terrace, three distinct, pronounced reflectors or interfaces that were common to all GPR profiles across the terrace. Furthermore, the three reflectors identified in each terrace were found to have similar GPR amplitudes and phases from one terrace to another and hence were uniform across the entire site. Figure 6 shows GPR images in a few example terraces (T1, T3, T6a, Figure 6a) and risers (R2, R4, R6b, Figure 6b).

[21] To extract the three identified reflectors from the global GPR data set, we first used the tracking tool of the OpendTect software, an open source interpretation system initially developed for seismic interpretation (<http://www.opendtect.org/>). The tracking of the three reflectors was performed for each profile in the depth domain (i.e., after topographic corrections and time-to-depth conversions had been applied to the data set). This process consists of profile-by-profile automatic picking of the reflector, starting on a few traces where the reflector has first been picked manually. The tracking tool then searches for the reflector on the adjacent traces using an amplitude criterion within a given thickness window, and automatically picks it. Note that we tested other attributes to pick the reflectors (instantaneous phase display and instantaneous amplitude display), but those tests showed only slight differences in the results and confirmed that the amplitude attribute was the most appropriate to automatically pick the reflectors.

[22] Reflector 1 (denoted Ref1 in the following) corresponds to the first and strongest continuous reflection observed in the 250 MHz GPR data (Figure 6). The first inset of the reflected signal is everywhere negative and this makes it easy to precisely pick the reflector using the automatic process described before. As shown in Figure 6a, Ref1 is found in each terrace, at a variable depth below the current ground surface, ranging from  $0.6$  to  $2.3$  m (errors are discussed in section 3.4). Ref1 is generally subhorizontal and by that roughly parallel to the ground surface. It loses coherency across most risers, although its trace may appear more or less continuous across a few of them (Figure 6b).

[23] Reflector 2 is the strongest reflector revealed in the 100 MHz GPR data (denoted Ref2 in the following; Figure 6). To extract it, we processed the 100 MHz GPR profiles with the classical filtering chain described in section 3.2, combined with a “predictive deconvolution process” performed to increase the resolution by refocusing the source signal whose duration was longer than one cycle. We also applied dynamic corrections made to simulate zero-offset data and to remove the moveout effects due to the  $2$  m offset between the emitting and the receiving antennas. We then conducted the automatic tracking and picking described before. As for Ref1, Ref2 is found in each terrace (Figure 6a), at a variable depth below the current ground surface, yet everywhere in the range of  $1$ – $3$  m (errors discussed in section 3.4). As for Ref1, it is basically subhorizontal and roughly parallel to the current ground surface. While its trace also loses coherency across a few risers, it more generally shows an apparent continuity across most of them (Figure 6b).

**a) Across terraces**



**b) Across risers**

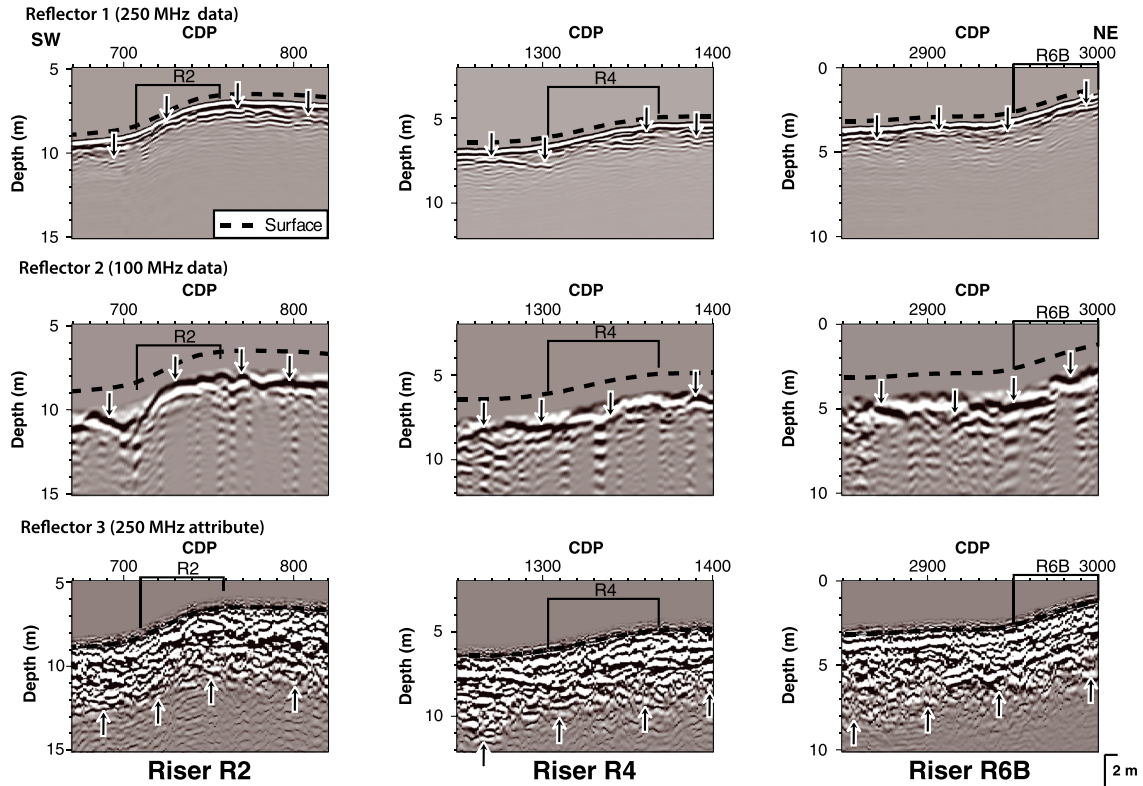


**Figure 6**

[24] The third interface (Reflector 3 or Refl3) coincides with a sudden and abrupt change in the GPR signal characteristics, essentially an abrupt disappearance of the reflected energy on both the 100 MHz and the 250 MHz data (Figure 6). The energy drop occurs at about the same depth on the 100 and 250 MHz data, in the range 2.7–6.9 m, and this shows that the energy disappearance is due to a pronounced change in the medium properties. Therefore, though Refl3 is not strictly speaking a reflector, it is certainly an actual physical, lithological interface in the medium that we may similarly extract. To pick this interface, we migrated the GPR data with a Stolt migration process [Stolt, 1978], mainly designed to enhance the energy drop (by focusing reflected energy and scattering noise energy). We then computed the second derivative of the envelope of the 250 MHz signals as this attribute enhances the visualization of the reflected events [Taner, 2001] and hence highlights the depth below which reflected events are no longer present. We performed this process on the 250 MHz data to take advantage of their highest resolution. The lowest limit of the envelope derivative was picked manually (Figure 6). The picking was then superimposed on both the 250 MHz and the 100 MHz data to check for the consistency of the results. The consistency revealed to be fair, showing that, although Refl3 is less clearly defined than the actual Refl1 and Refl2 reflectors, it is satisfactorily captured with our picking method. Refl3 was also found in each terrace, at a variable depth below the current ground surface, in the range 2.7–6.9 m (errors discussed in section 3.4). It is roughly horizontal and extends approximately parallel to the current ground surface (Figure 6a). It can be mapped continuously across the risers (Figure 6b).

[25] The three reflectors (or interfaces) were detected on all the GPR profiles, suggesting their spatial continuity both along and across the fault trace. However, we must keep in mind that the continuity that is revealed here is that of three reflectors (or interfaces) that have potentially similar electromagnetic property contrasts throughout the site. These similar electromagnetic property contrasts can be interpreted as being related to similar styles of subsurface material property contrasts. This does not imply that the natural features that show these contrasts are necessarily the same across the site. It is clear that they cannot be, as the investigated terraces have formed at different times over the Holocene. This will be discussed more thoroughly in section 4.2.

[26] The continuity of the three GPR reflectors allows us to interpolate each of them onto a  $2\text{ m} \times 2\text{ m}$  grid, identical to the one used to represent the ground surface topography. This allows us to produce three subsurface DEMs, each describing the paleo-topography of a specific GPR horizon (Figure 7).

### 3.4. Accuracy of the GPR DEMs

[27] The horizontal accuracy of the GPR-derived DEMs depends on: (1) the uncertainty on the profile locations that mostly comes from the separate GPS and GPR acquisitions, and reaches  $< 20\text{ cm}$ , (2) the heterogeneity in the spatial sampling performed every 20 cm along the fault and every 5 m across the fault, (3) the antenna frequency and the reflection depth, (4) the lateral resolution of the GPR images which is closely related to the Fresnel zone concept [Annan, 2009]. The later refers to how close two reflecting points can be in the horizontal plane and still be discriminated as two separate points. Taking into account all these factors, we estimate the lateral resolution ( $\Delta l$ ) on the GPR data to be  $\sim 50\text{ cm}$  for the Refl 1,  $\sim 1.1\text{ m}$  for the Refl 2, and  $\sim 1.1\text{ m}$  for the Refl3 ( $\Delta l = (\lambda z/2)^{1/2}$ , where  $z$  is the depth of the reflecting interface and  $\lambda$  is the wavelength of the center frequency; Cassidy, 2009). The features that are horizontally resolved on the  $2\text{ m} \times 2\text{ m}$  grid are thus robust (Figure 7).

[28] Uncertainties on depth values arise from both the variability in the wave velocities and the uncertainties on the static corrections (tied to GPS uncertainties). The CMP analysis suggests that the wave velocities vary in the range 10–14 cm/ns. We thus consider a mean velocity of 12 cm/ns associated with a  $\sim 20\%$  variability, and a  $\sim 20\text{ cm}$  uncertainty on the GPS vertical positions. Together these yield depth uncertainties on the GPR data in the range 23–50 cm for Refl1, 28–63 cm for Refl2, and 58–140 cm for Refl3 (20% of the depth range of the reflectors). The average depths that we find for the three GPR horizons are much beyond the vertical uncertainties. The higher-frequency “elevation” variations that are revealed in the Refl3 DEM (Figure 7) are certainly due to noise that results from the larger uncertainties on the picking and depth estimate for Refl3.

## 4. Stratigraphic Architecture of the Te Marua Terraces

[29] Figure 7 shows the DEMs of the current ground surface, Refl1, Refl2, and Refl3, illuminated from the NE, along with the mapping and labeling of the morphotectonic features that we identified (additional information is provided in the electronic supplements: zooms of Figure 7c allowing a clearer vision of markers and names (Figure S5a); the DEMs illuminated from the SW (Figure S5b); presented in slope gradients (Figure S5c); presented in slope directions (Figure S5d)). Figure 8 shows four topographic sections extracted from each DEM (shown with a 1:16 vertical exaggeration), taken either side of the fault (location on Figure 7c top). Table 1 lists the names of the

**Figure 6.** Example GPR profiles showing close-up views of the three principal GPR reflectors that we have extracted. (a) GPR profiles in three example terraces; (b) GPR profiles across three example risers. In Figures 6a and 6b, the  $x$  axis is the Common Depth Points (CDP) increasing eastward, with a 20 cm spacing between each CDP number; the  $y$  axis is the depth in meters. In all plots, the dotted line represents the ground surface. The blind zone below the ground surface is due to the suppression of direct waves. On 250 MHz GPR data, arrows indicate Reflector 1; on 100 MHz GPR data, arrows indicate Reflector 2; on the image of the second derivative envelope computed from the 250 MHz data, arrows indicate Reflector 3. Reflector 3 corresponds to an abrupt decrease in the energy represented on the plot to the right, where the black and gray lines show the mean of energy over the section for the 250 and the 100 MHz data, respectively. The light gray band represents the depth range of reflector 3.

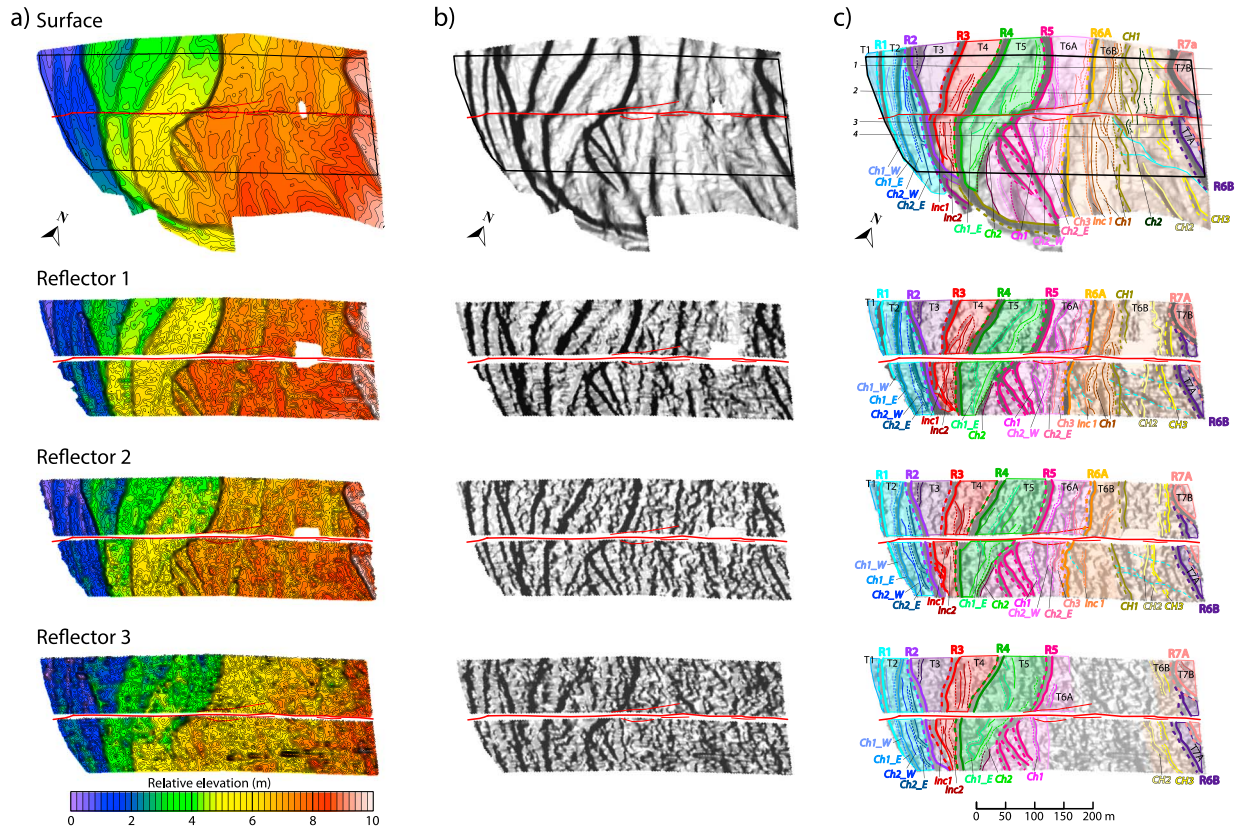


**Figure 7.** GPS- and GPR-derived DEMs, and mapping of alluvial and morphological markers. From top to bottom, we present the DEMs of the ground surface, of the Reflector 1, of the Reflector 2, and of the Reflector 3. In all plots, the DEMs are illuminated from the NE; the red line represents the fault trace. (a) Contour map with colors depicting relative elevation. Contour lines are represented every 20 cm. (b) Hillshape sunlit DEM in gray tones. (c) Map of the markers identified in each DEM. Color zones discriminate the different terraces. Terrace and riser names are indicated. Smaller markers are named depending on the nature of the marker (“Ch” and “CH” for channels, minor and larger, respectively; “Inc” for incision of less clear origin) and their number increases from west to east within each terrace. Note that we mapped the topographic features that were best revealed in the DEMs, and whose lateral offsets were clear. Solid and dotted lines indicate the top and base of markers, respectively, wherever those bases and tops could be mapped. The two facing flanks of a channel may have their bases not exactly superimposing, in cases where streambeds has a resolved width. W and E refer to west and east flanks, respectively. Black lines 1–4 are cross sections shown in Figure 8. Black rectangle is the zone covered with GPR data. Additional information, especially zooms allowing a better vision of the markers, is provided in the supporting information (Figure S5).

landforms that we identified and compares them to those previously reported in the literature.

#### 4.1. Present Terrace Landforms

[30] Because our DEM of the ground surface covers a wider area than the previously available DEMs (Figure 5) [Little *et al.*, 2010], it provides a more complete image of the current surface at Te Marua.

[31] The Wellington fault trace appears remarkably linear and, with the exception of a small push-up in the fault center, is associated with no or very little tectonic scarps. The projection of the terrace trends across the fault reveals no vertical displacement, which confirms that the fault has a purely strike-slip motion at Te Marua [e.g., Berryman, 1990; Gross *et al.*, 2004; Little *et al.*, 2010].

[32] As described in prior works, the current Te Marua morphology is shaped by a flight of alluvial terraces (colored areas

in Figures 7 and 8). Though most of the risers and terraces are dextrally displaced by the fault, their respective continuity is preserved across the fault, making their recognition relatively straightforward. Toward the east, away from the current Hutt riverbed, the terrace trends increase in elevation across each riser, all in all accounting for a total change of about 10 m over a distance of about 600 m (Figure 8). R5 is the highest (~3 m) and most prominent riser at surface. It separates the site in two parts. West of R5, toward the current riverbed, risers R1 to R5 are remarkably steep, sharp, continuous, and quite high (generally  $\geq 1$  m), while the terrace trends are quite flat, with most dipping slightly toward the east (Figure 8). These western, youngest terrace trends are dissected by abandoned channels and incision features, most have a well-defined linear shape. The second highest riser is R2 (~2 m, Figure 8). East of R5, a large area extends from R5 to the base of R6b–R7a, which lacks any pronounced relief (Figure 7). A few clear

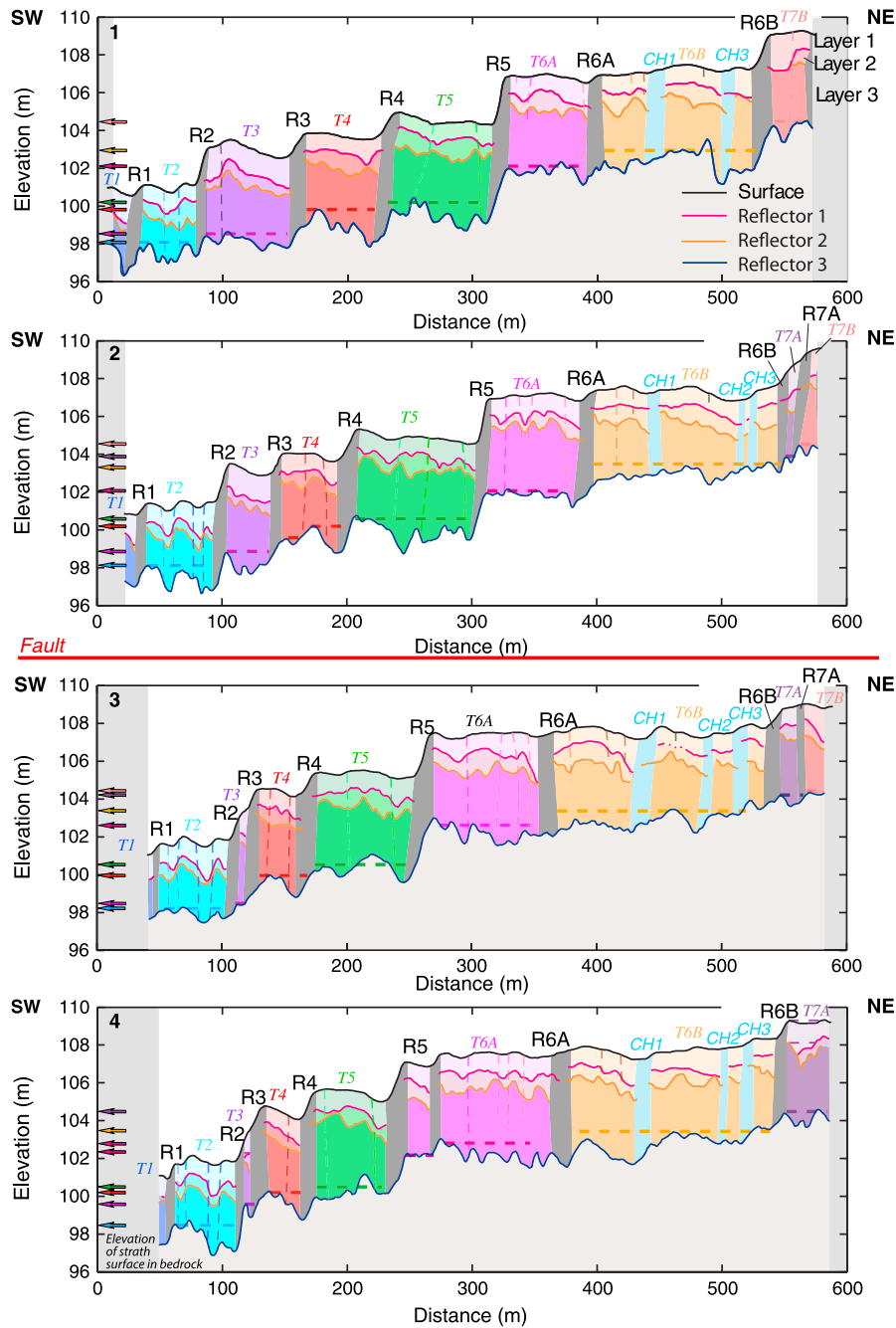


**Figure 8.** Topographic sections across the four DEMs, chosen either side of the fault (location in Figure 7c). Profiles extracted from surface (black), Reflector 1 (pink), Reflector 2 (orange), and Reflector 3 (dark blue) are superimposed, with vertical axis indicating elevation. Color zones discriminate the different terraces. The riser scarps that separate the different terraces are represented in gray. The step arrangement of the terraces, visible in the four horizons, is suggested with horizontal dotted lines on Ref3 (strath surface) and reported as arrows to the left. Names are indicated for terraces, risers, and major channels CH*i*. Thin dotted lines locate the more minor features mapped in Figure 7.

morphological features exist however, among which the most pronounced have been labeled R6a, CH1, CH2, and CH3. Although R6a is smoother and less continuous than the risers in the west, with a height of at most 1–1.5 m, it forms a clear west-facing step in the topography (Figure 7), which suggests that R6a is a small terrace riser. In contrast, it is not clear whether CH1, CH2, and CH3 are eroded risers or stream channels. Although their eastern “flank” is generally steeper and

higher than their western edge, the topographic differences are small, and hence we interpret them as abandoned and eroded channels. Finally, risers R6b and R7a form two pronounced topographic steps in the east of the site. The sharpness, steepness, and height of these two risers are similar to those of R5.

[33] All in all, we identified 23 offset markers with a clear continuity across the fault (8 west-facing risers, 12 abandoned

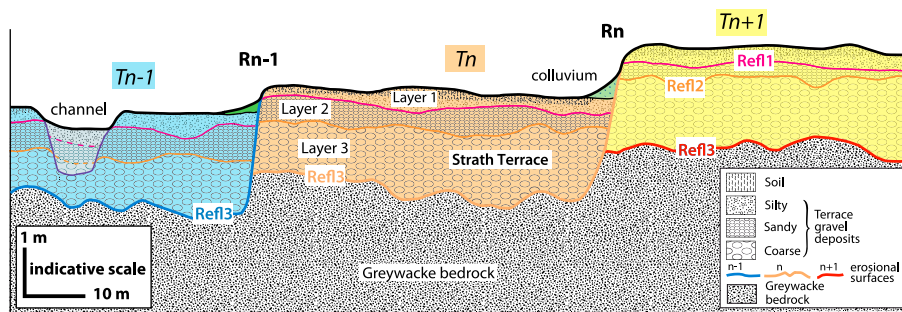


**Figure 9.** Synthetic representation of the Te Marua alluvial terrace architecture that is revealed from GPR data. The three GPR reflectors are allostratigraphic horizons that separate gravels of different grain sizes and compositions. Refl3 is the erosional strath surface in the greywacke bedrock. Both the GPR reflectors and the layers in between are different and diachronous from one terrace to another (note that they have dissimilar thicknesses); yet they show similar GPR properties and facies throughout the Te Marua site and as such are allostratigraphic units that can be mapped continuously. Since they were formed, the riser scarps have been partly weathered at the current ground surface (as suggested by the colluvium in green), whereas the risers have remained better preserved and hence steeper in the subsurface layers.

stream channels, and 3 erosional features of less clear origin). This is more than reported so far (Table 1).

#### 4.2. Nature of the GPR Horizons and Vertical Architecture of the Terraces

[34] The three GPR horizons have an overall topography and morphology that are both similar to those of the current ground surface (Figures 7, 8). Each GPR horizon is shaped in steps that increase in elevation from west to east, and these steps coincide with the successive terrace treads and risers observed at surface. It is thus clear that each GPR horizon is not a continuous surface, but instead a patchwork of distinct and separate alluvial surfaces (colored areas in Figures 7c and 8). Therefore, we observe that each Te Marua terrace is a multilayer pile that includes at least four roughly parallel, subhorizontal horizons, a fairly deep horizon, Refl3, that extends at 2.7–6.9 m below the current ground surface, two shallower horizons, Refl2 and Refl1, that lie below the present ground surface at 1–3 m and 0.6–2.3 m, respectively, and the surface tread itself that forms the current land surface. Together these suggest that Refl1, Refl2, and Refl3 might be stratigraphic boundaries within the alluvial terraces.

[35] Stratification of alluvial degradation terrace deposits is a common observation (Figure 2) [e.g., Wegmann and Pazzaglia, 2002], though we know no study that documents the 3D architecture of such terraces. The deposits are typically made of a succession of well-sorted gravels and sands that are several meters thick (usually 3–5 m) [e.g., Bull, 1990; Merritts and Hesterberg, 1994] and that fine upward (Figure 2) [Merritts and Hesterberg, 1994; Pazzaglia, 2013]. With this common behavior in mind, we attribute the identified reflectors (Refl1–Refl3) with stratigraphic contacts.

[36] The deepest Refl3 horizon corresponds to a transition between a resistive (i.e., reflective) medium and a deeper more conductive layer. Gross *et al.* [2004] also observed an abrupt change in the reflection pattern at a similar depth, and interpreted it as the sediment/bedrock contact. As reported in section 2, the greywacke bedrock might lie at shallow depths at Te Marua. Because it is markedly weathered, the greywacke bedrock is expected to have a large electrical conductivity [von Borstel and Ingham, 2004] that,

in turn, is expected to strongly attenuate GPR signals. Therefore, we concur with Gross *et al.* [2004] that Refl3 corresponds to the sediment/bedrock interface (Figure 9). The existence of the Refl3 horizon below each of the terraces shows that all the T1–T7b Te Marua terraces are strath terraces carved into the bedrock at different times during the Holocene. The stepped arrangement of the Refl3 surfaces is in keeping with this inference (Figure 8).

[37] We interpret the layer in between the Refl3 and Refl2 horizons (referred to as layer 3, Figure 9) to be, in each terrace, the bed load coarse gravels that were transported and emplaced when the terrace straths were cut (Figure 2) [e.g., Bull, 1990; Wegmann and Pazzaglia, 2002]. The thickness of this layer varies among the terraces, from 60 cm to 5 m (supporting information Figure S6 where thicknesses of layers 1, 2, and 3 are mapped).

[38] From trenches, Langridge *et al.* [2011] report that the T1, T2, and T3 terraces are made of a ~1.5 m thick sandy material sitting on a bouldery unit. Little *et al.* [2010] additionally report that most of the terraces are mantled by a 0.8–1 m thick layer of coarse to fine sand. The Refl1 horizon extends to a depth that more or less coincides with the transition between shallow sandy material and deeper coarser bouldery material. It is thus likely that the Refl1 GPR reflection corresponds to this material contrast, at least in the western part of Te Marua, whereas the Refl2 reflector might correspond to the base of the coarse cobble-to-boulder alluvium layer that is seen at the bottom of the trenches. Both layers 1 (between current land surface and Refl1, Figure 9) and 2 (between Refl1 and Refl2, Figure 9) show a variable thickness among the terraces that ranges between a few tens of cm and ~3 m, and between a few tens of cm and ~2 m, respectively (Figure S6).

[39] Figure 9 synthesizes the stratigraphic architecture of the Te Marua terraces that we infer from the GPR data combined with trench and field observations. Although physically contiguous and mappable as allostratigraphic units (i.e., lithologically similar deposits; e.g., Bull, 1990; Seidl and Dietrich, 1993; Merritts and Hesterberg, 1994), the terraces are diachronous; the carving of each strath occurred at different times during the Holocene. The similarity

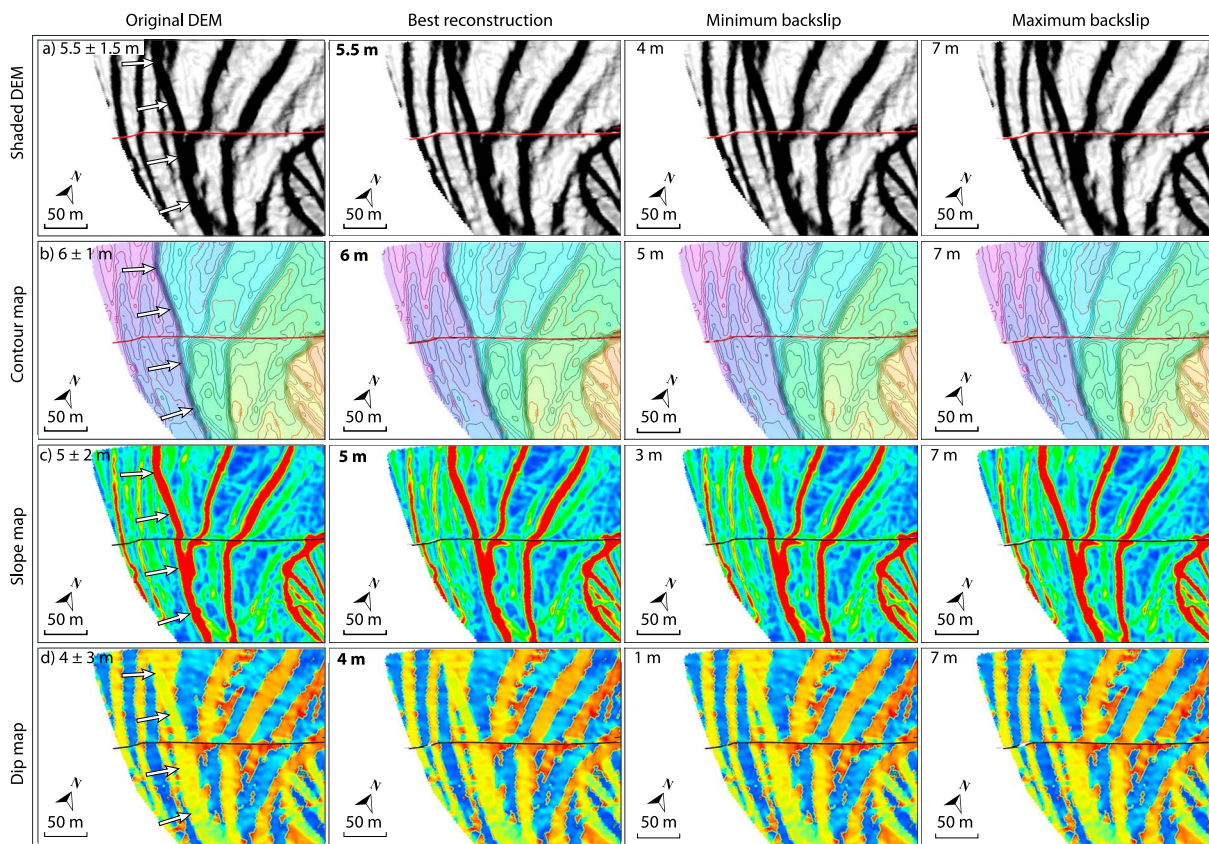


**Figure 10.** Example of back slip reconstructions showing how uncertainties on offset measurements are determined. The chosen case is that of riser R2 (base) which is documented on the surface DEM. First panel, actual DEM; second panel, back slip reconstruction yielding the best offset; third panel, back slip reconstruction yielding the minimum plausible offset; fourth panel, back slip reconstruction yielding the maximum plausible offset. In each panel, the back slip is done on the four representations of the topographic data, (a) hillshade sunlit, illuminated from the NE, (b) contour lines, (c) slope map (color scale in Figure S5), (d) dip map (color scale in Figure S4). The offsets are indicated, in bold for the preferred value (see Table S1 in supporting information).

of the GPR facies of the different terraces suggests, however, that those terraces were formed in a similar manner. Each time, the carving of the bedrock was accomplished by a fairly thick, coarse gravel facies layer 3 which became preserved atop the strath [e.g., Bull, 1979; Seidl and Dietrich, 1993; Hancock and Anderson, 2002]. By the end of this graded process, each terrace was mantled with thinner and finer alluvium such as we see forming layers 1 and 2. These fine-grained alluvial facies represent vertical accretion processes atop the flood plain, and some of these processes might have occurred during floods [e.g., Wegmann and Pazzaglia, 2002]. Each strath formation eventually ended with stream-channel incision back into the strath. Each vertical incision produced a riser that offsets and hence intersects the subhorizontal stratigraphic layers that constitute the previous terrace. The deposits of the subsequent strath terrace overlap the riser so that the stratigraphic boundaries from one terrace to the next may appear as fairly connected, even though they are not. This is likely the main reason why the GPR reflectors can be picked roughly continuously throughout the entire site, including across most of the risers (Figure 6b). That distinct terraces exhibit a similar architecture may result from these terraces having formed closely

spaced in time [e.g., Bull, 1990], in a period during which the dynamics of the Hutt River was basically the same.

## 5. Fault Offsets of the Te Marua Terraces

### 5.1. Offset Measurements and Uncertainties

[40] As a consequence of the way they formed, the risers mapped at surface can be recognized in the three GPR horizons (Figure 7). Furthermore, most of the channels and other erosional features that incise the terraces at the surface are found to incise all the way down to the Refl2 or Refl3 horizons. Only in the eastern part of Refl3 between R5 and R6b are the alluvial markers more ambiguous to identify, due to the lower resolution of the Refl3 GPR data. Of the 23 landforms that we mapped either side of the fault at the current ground surface, 21 are identified in Refl1, 20 in Refl2, and 13 in Refl3 (Table S1 in supporting information). This allows us to observe the respective markers at three to four different depths and therefore to measure their lateral offsets three to four times. The subsurface GPR data thus provide an important contribution to the fault slip determination: first, by allowing a densification of the measurements, they contribute to more tightly define the fault offsets and their uncertainties;

second, by providing measurements independent from those derived at the current ground surface, they allow examining whether the recovered offset values show any variability from subsurface to surface.

[41] We first measured the fault offsets separately in each DEM, following a common procedure. In each horizon, most markers have a clear expression on either side of the fault trace, so that the correlation of their two offset sections across the fault is generally unambiguous. However, as there are a few cases where the correlation might be partly ambiguous, we assign a quality weight to each offset measurement that qualifies the trust that we have in the correlation of the two marker sections (Table S1 in supporting information). The weight is 1 for unambiguous correlations and assigned to 0.5 for the correlations that might be slightly ambiguous. The weight is lowered to 0.3 for a few rare cases in the eastern part of the site where the marker traces are less clear. Where the correlation is too ambiguous, we ignore it (e.g., eastern part of Refl3; Table S1 in supporting information).

[42] The lateral offset recorded by two separated marker sections is then determined by restoring—through an along-fault back slip process—the most likely original position and shape of the marker. To perform such measurement, we followed the steps below.

[43] First, as most of the markers form scarps (risers and stream edges), wherever possible, we mapped the top and base of those scarps and measured the offset both across the top and across the base of the scarp.

[44] Second, we examined each marker and measured its lateral offset on four different views of the data (Figures 7 and ES5): (1) a sunlit, hill-shade representation of the topography helps to reveal much of the topographic relief, even small, thereby allowing a clear assessment of the offset features; (2) a contour line representation of the topography provides a quantitative guide to reconstruct the original shape of the markers. As there is no vertical slip on the fault at Te Marua, such a representation is especially relevant to restore the original shape of the markers near the fault trace; (3) a slope representation of the topography highlights the markers that have the steepest scarps, independent of their sense of dip. That representation is especially relevant to reconstruct the original shape of the most pronounced features; (4) a dip representation of the topography both images the dips and slopes of all the topographic scarps, even small. This representation thus complements the previous one by providing details on the features that have gently dipping scarps. The combination of these four representations of the topographic data allowed us to better embrace and define the overall traces of the markers (i.e., long, “average” traces smoothing out local, small fluctuations, see Figures 10, 14, and ES7 further below), and to restore those traces across the fault. Note that, because we correlated the overall traces of the markers, the offset measurements that we performed are not biased by the local complexities that might exist in the immediate vicinity of the fault trace, or by the lack of GPR data in that near-fault zone (Figures 5 and 7).

[45] We have measured the top and base of every offset marker, on these four representations (wherever it was possible to do so), so that, eventually, each marker has its lateral offset measured eight times at best (Table S1 in supporting information). Figure ES7 shows a few examples of markers reconstructed on one or other data representation. Each offset

measurement comes with an uncertainty that quantifies the range of offsets that would yield a plausible reconstruction of the original marker. Figure 10 provides one example of such a reconstruction with the estimation of the uncertainty. Overall, the uncertainties reveal to be small in the western and hence youngest part of the site (west of ~R3), on the order of 1–2 m, whereas they are larger further east, on the order of 3–4 m (Table S1 in supporting information).

[46] To further constrain the fault offsets and their uncertainties, the various measurements performed for a given marker (up to 8) are averaged (column “mean” in Table S1). The resulting means are the values that we take as best measuring the offsets, and hence those that we consider in the following analysis. The overall uncertainties  $\sigma$  on these mean offset values are calculated by propagation of uncertainty as  $\sigma = [1/(N-1)(\sigma_1^2 + \sigma_2^2 + \dots + \sigma_N^2)]^{1/2}$  with  $N$  denoting the number of measurements and  $\sigma_i$  the uncertainty on the measurement  $i$  (i.e., offset range) [Taylor, 1997]. The uncertainties that result from averaging multiple measurements are generally in the range 1–3 m (Table S1).

[47] Finally, in each horizon, we represent the entire collection of mean offset values as a probability density function (PDF) [e.g., McGill and Sieh, 1991; Lowell, 1995; Zielke et al., 2010; Beaupretre et al., 2012]. Each individual mean offset is represented with a Gaussian distribution. The center of each Gaussian is one mean offset value while its standard deviation ( $\pm 2 \sigma$ ) is the uncertainty on the offset (Table S1). Each individual PDF is weighted by the factor that qualifies the robustness of the correlation between the paired markers (Table S1) [Zielke et al., 2010]. Summing the individual PDFs then highlights “peaks” that indicate which are the most common and/or the most precise values within the entire data collection. The peaks are as high as the offset is well represented, and as narrow as the uncertainty on the offset is smaller. In this way, the best constrained offset values can be robustly extracted.

## 5.2. Offset Analysis

[48] Figure 11 shows the lateral offsets plotted as a function of their distance from the present riverbed, with colors discriminating the horizons where the offsets were measured. The four horizons exhibit a fairly similar slip record. Yet, the offset values measured at the ground surface are generally lower than the corresponding displacements measured in the subsurface. All in all, the offsets progressively increase away from the river. While this increase is expected for the riser offsets due to the arrangement and relative age of the terraces, it is more surprising that the channels and other features that incise the terrace treads show the same pattern. This suggests that those features formed at about the same times than the surface treads which they incise, and that no “recent” channel incised the terrace treads later after their formation.

[49] Figure 12 shows the offset values measured at the ground surface (Figure 12a), in Refl1 (Figure 12b), in Refl2 (Figure 12c), and in Refl3 (Figure 12d), as individual PDFs (black lines), as a summed PDF curve (red line), and as a histogram (gray bars).

[50] At surface, the slip record includes 26 measurements and is in the range 1.5–37 m (Table S1 in supporting information). One high and narrow peak shapes the summed PDF curve, thereby revealing a well-constrained offset value at ~6.1 m. The summed PDF curve shows another zone of fairly

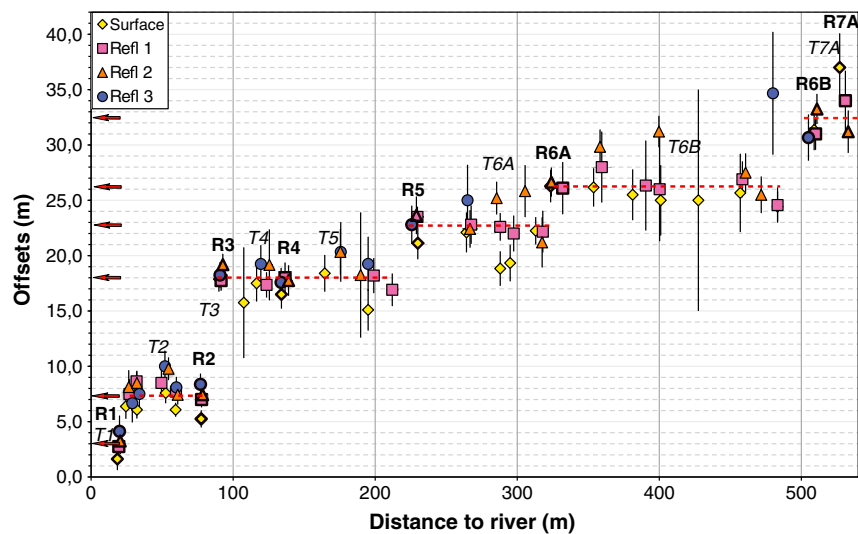


**Figure 11.** Lateral offsets as a function of their distance to the present riverbed. Offsets are mean values in Table S1 in supporting information. They are shown with their uncertainties. Symbols for riser offsets are highlighted in bold while the names of the risers are indicated also in bold. Terrace names are in italic. Red dotted lines suggest a specific grouping of the offsets. The corresponding approximate, average offsets are indicated with arrows on the left.

large PDF values, in the slip range 15–27 m. There, three peaks can be distinguished, a quite narrow and clear peak at  $\sim 17.8$  m, and two smoother peaks at  $\sim 22.2$  and  $\sim 25$  m. The smoothness of the  $\sim 22$  and  $\sim 25$  m peaks arises from the large overlaps that exist between the offset data when their uncertainties are taken into account. It suggests that the  $\sim 22$  and  $\sim 25$  m offsets are not well discriminated from one another. Finally, the summed PDF curve shows a small peak at  $\sim 1.6$  m, which arises from one single measurement. The 1.6 m offset is thus poorly constrained. Therefore, though we measured 26 distinct offsets at the ground surface, only two offset values are robustly supported, at  $\sim 6.1$  and  $\sim 17.8$  m, whereas two more offsets are suggested at  $\sim 22.2$  and  $\sim 25$  m. The uncertainties on these offset values are difficult to estimate since the peaks in the summed PDF curve are not a Gaussian or any specific mathematical function. However, uncertainties of  $\pm 1$ – $2$  m well cover the full range of the actual measurements that combine to produce each of the peak values.

[51] In Refl1 (Figure 12b), the slip record includes 24 measurements and is in the range 2.8–34 m, similar to the surface measurements. The summed PDF curve shows three high and narrow peaks, thereby revealing three well-defined offsets at  $\sim 7.6$ ,  $\sim 17.7$ , and  $\sim 23.3$  m ( $\pm 1$ – $2$  m, as before). An additional small peak is identified at  $\sim 2.8$  m. It arises from a single measurement, however, and hence, is more poorly constrained.

[52] In Refl2 (Figure 12c), the slip record includes 23 measurements and is in the range 3.3–33 m. The summed PDF curve shows four high and well-distinct peaks, which suggest that four well-constrained offset values emerge from the data collection, at  $\sim 7.7$ ,  $\sim 19.1$ ,  $\sim 26.2$ , and  $\sim 30.7$  m ( $\pm 1$ – $2$  m). An additional yet more poorly constrained offset is suggested at  $\sim 3.3$  m.

[53] Finally, in Refl3 (Figure 12d), 15 measurements are available that are in the range 4–35 m. The summed PDF curve shows two high and narrow peaks, which reveal two

well-constrained offsets at  $\sim 8.1$  and  $\sim 18.2$  m ( $\pm 1$ – $2$  m). An additional yet less constrained offset is suggested with a small peak at  $\sim 22.5$  m.

[54] Figure 13a now compares the four data sets, while Table 2 compares the offsets per marker among the different horizons. Together these documents show that most of the offset values measured at the ground surface are lower than those measured in the subsurface horizons. Therefore, independent on the reasons why the surface record differs from the buried GPR record (see discussion in section 6.1), we build Figure 13b which shows all the offset data except those at the surface. The resulting summed PDF curve shows three clear peaks that reveal three well-constrained offsets at  $\sim 7.8$ ,  $\sim 18.1$ , and  $\sim 23.3$  m. The curve also exhibits three smaller and/or smoother peaks which suggest that three more offsets are recorded, yet less clearly, at  $\sim 3.2$ ,  $\sim 26.3$ , and  $\sim 30.5$  m. Five of the six above values are larger by 1–1.5 m than those measured at the current ground surface (Figure 13c).

## 6. Discussion

### 6.1. Defining the Best Constrained Slip Record: Relative Contribution of Surface and GPR Data

[55] Table 1 synthesizes the surface offsets reported in the literature [Little *et al.*, 2010; Berryman, 1990; Lensen, 1958] and compares them to those we obtained in the current landforms. With the exception of a few values, most measurements agree within uncertainties or differ by less than a meter. The “integrative” well-constrained offsets that we find ( $\sim 6.1$ ,  $\sim 17.8$ ,  $\sim 22.2$ , and  $\sim 25$  m, each with an uncertainty of  $\pm 1$ – $2$  m) are also similar to those previously reported ( $5.3 \pm 0.8$ ,  $14.3 \pm 3.1$ , and  $20.1 \pm 1.2$ ; Berryman [1990], Little *et al.* [2010]), although we suggest an additional offset at  $\sim 25$  m. Only two significant differences exist between available and present measurements. First, a large,  $\sim 10$  m difference is found in the offsets of the two easternmost risers, R6b and R7a. This arises from a different interpretation of the marker

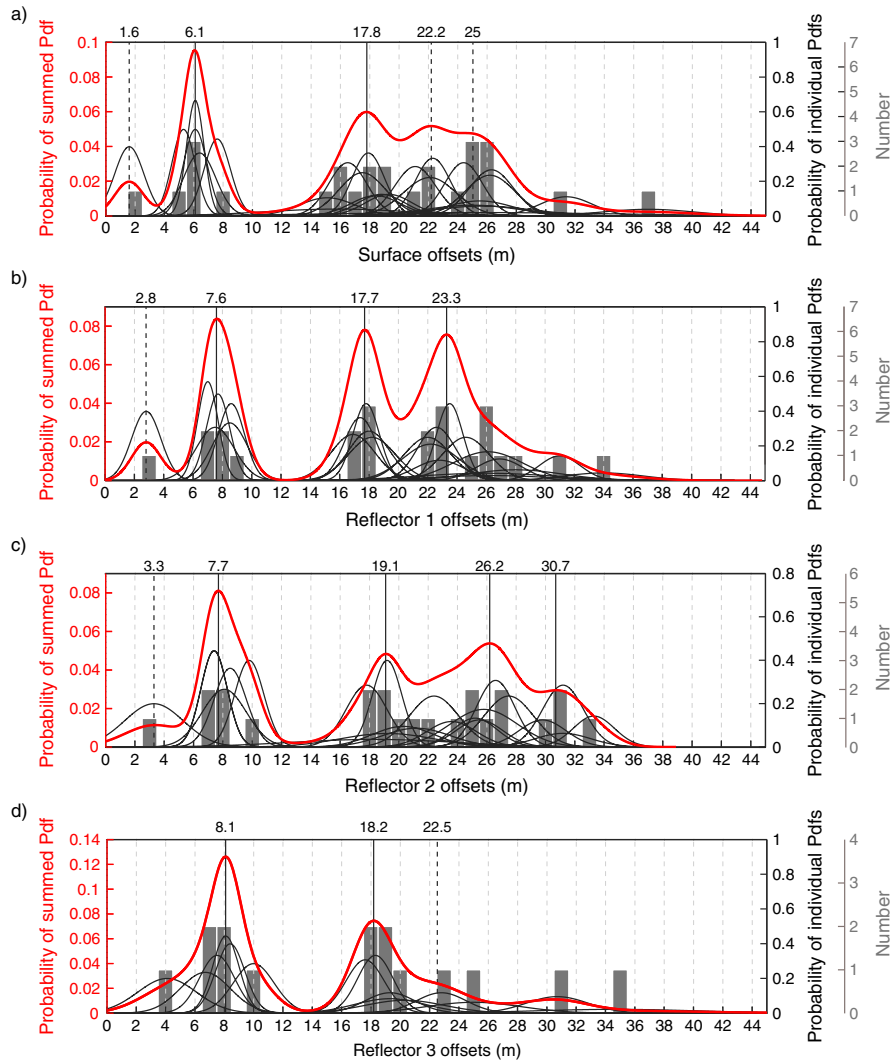


**Figure 12.** Probability density analysis (PDF) of the offsets measured in the four horizons, at the (a) ground surface, (b) for Refl1, (c) for Refl2, and (d) for Refl3. In each plot, offsets are mean values in Table S1 in supporting information. Each offset is represented as an individual, Gaussian PDF (black, right axis). Offsets are also shown as a histogram (black bars, right axis). The summed PDF curve is shown in red (left axis). The best constrained offsets derived from the summed PDF curve are indicated above vertical lines. These lines are dotted for the values that are less well constrained.

sections to be correlated; while we reconstructed the overall, 100–150 m long traces of the R6b and R7a risers on either side of the fault (see Figure S7i–j), *Little et al.* [2010] reconstructed shorter, 20–50 m long sections nearby the fault. We note that the next offset to the east measured by *Little et al.* [2010] (not surveyed in our DEM) is  $21.8 \pm 10.7$  m, consistent within uncertainties with the R6b and R7a offsets that we measured. Second, a significant difference is found in the determination of the smallest offset. All previous studies report that the youngest R1 riser is not offset by the fault. By contrast, as shown in Figure 14a, our surface data suggest that 1–1.5 m of lateral slip might have contributed to displace the two current sections of R1 on either sides of the fault (note that Figure 14 has been built at 1 m resolution). This finding is not strongly constrained, however, as it relies on one single measurement, with uncertainties almost as large as the offset. We expand on this smallest slip further below.

[56] GPR data provide additional constrains to refine the offset record. Overall, the best constrained offsets recovered from the GPR data are similar to those measured at the ground surface. Yet they are systematically a bit larger, generally by 1–1.5 m (Figure 13c). That such a difference is systematic suggests that it does not result from larger horizontal uncertainties on the GPR data. The ground surface is the site of significant weathering and deposition. It is common that surface scarps have their crest rapidly eroded and smoothed (by rain, wind, temporary gullies, human activities, etc.), whereas their base becomes buried by the eroded material (Figure 9). Furthermore, the Hutt River might have overflowed its bed at various times during the Holocene as it does nowadays from time to time [*Little et al.*, 2010]. The overflows might have mantled the ground surface with thin silty sediments (not discriminated within GPR layer 1; suggested to be ~40 cm in *Little et al.* [2010]) that would then partly smooth the existing morphological features. Therefore, as a consequence of the

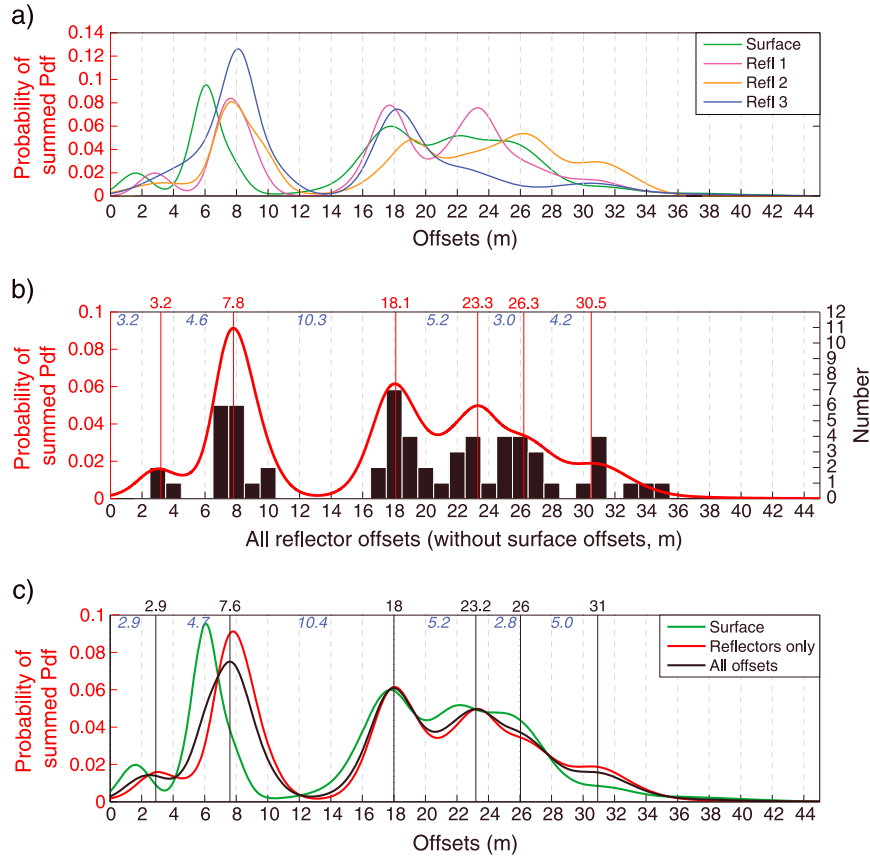


**Figure 13.** Comparison of the four slip data sets. (a) The four summed PDF curves (from Figure 12). (b) Summed PDF curve and histogram of offsets derived from the GPR data alone (Refl1, Refl2, and Refl3). Best constrained offsets are indicated in red. Slip increments between these offsets are in blue italic. (c) Comparison of the summed PDF curves obtained for the surface data (green), for the GPR data (red), and for all surface and subsurface data (black). Best constrained offsets derived from the entire data set are indicated in black, while the slip increments that separate them are in blue italic.

dynamic processes that it sustains, the current ground surface might provide a slightly modified image of the original alluvial markers and of the offsets they have recorded. By contrast, since they are interbedded within the alluvial pile of each terrace, the stratigraphic horizons imaged in the GPR data are better preserved from subsequent erosion. The original shape of the risers that separate these horizons from one terrace to the next is thus well preserved, as are the fault offsets that these “buried” risers have recorded.

[57] The offsets measured in the GPR data might thus be closer from the actual fault slips than those measured at the current ground surface. If we consider only the GPR data, we infer that the Te Marua terraces record six cumulative lateral fault slips, three are robustly constrained at 7.8, 18.1, and 23.3 m, whereas the three others, at  $\sim 3.2$ ,  $\sim 26.3$ , and  $\sim 30.5$  m, are less well constrained although generally represented by many measurements. Each offset has an uncertainty of about 2 m (Figure 13b). If, conversely, we consider that the surface data are as valuable as the subsurface measurements, we conclude that the Te Marua terraces have recorded six cumulative lateral fault slips, of  $\sim 2.9$ ,  $\sim 7.6$ ,  $\sim 18.0$ ,  $\sim 23.2$ ,  $\sim 26.0$ , and  $\sim 31.0$  m (each  $\pm 2$  m, Figure 13c). As the findings are similar whether one or other hypothesis is chosen, we use in the following the most cautious result that integrates the entire surface and subsurface data collection.

[58] The smallest offset across R1 is present in the four data sets, thereby strengthening its existence. Figure 14 shows the reconstruction of riser R1 (at 1 m resolution), on the different DEM reflector levels. In each level, the riser strikes differently on either side of the fault trace, suggesting that its overall shape, “averaged” on long sections (dotted lines in Figure 14), is slightly curved with a concavity toward the East. The two lines that represent the average strike of R1 either side of the fault trace do not intersect across the fault. At surface, a back slip of  $\sim 1.5$  m is needed to make the two lines connecting across the fault, whereas, in the subsurface, a larger back slip of 3–4 m is suggested. Therefore, as with most other offsets, this smallest slip event shows larger values in the GPR data. For the reasons discussed above, we suspect that the R1 offset might be better preserved in the subsurface while subsequent erosion and/or burial might have partly smoothed it off in the current land surface. This would explain why the smallest R1 slip is hardly presently detectable at the surface and effectively has not been detected in prior surface analyses [Berryman, 1990; Van Dissen et al., 1992, Little et al., 2010]. We note that, if the 3–4 m R1 offset was not real, we would have to admit that the smallest slip recorded at Te Marua is  $7.6 \pm 2$  m (Figure 13c). Such a 7.6 m offset is likely too large to result from a single earthquake event on a mature fault as is the Wellington fault

**Table 2.** Comparison of the Mean Offset Values (in Bold) Estimated, for Each Marker, on the Four DEMs

	Surface	Ref1	Ref2	Ref3
<b>R1</b>	<b>1.6</b> ±1.0	<b>2.8</b> ±1.0	<b>3.3</b> ±2.0	<b>4.1</b> ±2.0
T2-Ch1_W	<b>6.4</b> ±1.1	<b>7.5</b> ±1.3	<b>8.1</b> ±1.5	<b>6.7</b> ±1.7
T2-Ch1_E	<b>6.1</b> ±0.8	<b>8.6</b> ±0.9	<b>8.5</b> ±1.1	<b>7.5</b> ±1.2
T2-Ch2_W	<b>7.6</b> ±0.9	<b>8.5</b> ±1.2	<b>9.8</b> ±1.0	<b>10.0</b> ±1.4
T2-Ch2_E	<b>6.1</b> ±0.6	<b>7.7</b> ±0.8	<b>7.4</b> ±0.9	<b>8.1</b> ±0.9
<b>R2</b>	<b>5.3</b> ±0.8	<b>7.0</b> ±0.7	<b>7.4</b> ±0.9	<b>8.4</b> ±1.0
<b>R3</b>	<b>17.9</b> ±1.1	<b>17.8</b> ±0.9	<b>19.2</b> ±1.0	<b>18.3</b> ±1.2
T4-Inc1	<b>15.8</b> ±5.0	-	-	-
T4-Inc2	<b>17.5</b> ±1.6	<b>17.4</b> ±1.1	<b>19.2</b> ±3.2	<b>19.3</b> ±1.7
<b>R4</b>	<b>16.5</b> ±1.3	<b>18.0</b> ±1.4	<b>17.8</b> ±1.4	<b>17.6</b> ±1.3
T5-Ch1_E	<b>18.4</b> ±1.7	<b>18.2</b> ±1.6	<b>20.3</b> ±2.1	<b>20.3</b> ±2.7
T5-Ch2	<b>15.1</b> ±1.9	<b>16.9</b> ±1.5	<b>18.3</b> ±5.7	<b>19.3</b> ±2.4
<b>R5</b>	<b>21.1</b> ±1.4	<b>23.5</b> ±0.9	<b>23.6</b> ±1.7	<b>22.8</b> ±1.7
T6a-Ch1	<b>22.1</b> ±1.8	<b>22.8</b> ±1.7	<b>22.4</b> ±1.7	<b>25.0</b> ±3.2
T6a-Ch2_W	<b>18.8</b> ±1.6	<b>22.6</b> ±1.3	<b>25.2</b> ±1.5	-
T6a-Ch2_E	<b>19.3</b> ±1.6	<b>22.0</b> ±1.6	<b>25.8</b> ±2.3	-
T6a-Ch3	<b>22.3</b> ±1.2	<b>22.2</b> ±1.9	<b>21.2</b> ±2.3	-
<b>R6A</b>	<b>26.3</b> ±1.5	<b>26.1</b> ±2.4	<b>26.6</b> ±1.3	-
T6b-Inc1	<b>26.2</b> ±1.7	<b>28.0</b> ±3.2	<b>29.8</b> ±1.6	-
T6b-Ch1	<b>25.5</b> ±2.3	<b>26.3</b> ±4.1	-	-
T6b-CH 1	<b>25.0</b> ±3.2	<b>26.0</b> ±4.7	<b>31.2</b> ±1.4	-
T6c-Ch1	<b>25.0</b> ±10.0	-	-	-
T6b-CH2	<b>25.7</b> ±3.5	<b>26.9</b> ±1.6	<b>27.5</b> ±1.7	<b>34.7</b> ±5.5
T6b-CH3	<b>24.4</b> ±1.3	<b>24.6</b> ±1.6	<b>25.5</b> ±1.6	-
<b>R6B</b>	<b>31.4</b> ±1.8	<b>31.0</b> ±1.4	<b>33.3</b> ±1.4	<b>30.7</b> ±2.1
<b>R7A</b>	<b>37.0</b> ±3.1	<b>34.0</b> ±2.7	<b>31.2</b> ±1.9	-

(see updated earthquake scaling relations in *Manighetti et al.* [2007]; the 7.6 m value is especially too large as it is a local slip value along the fault, and hence a slip value that is likely lower than the maximum coseismic slip produced by the most recent event). Therefore, we suggest that the smallest and youngest slip recorded at Te Marua is 3–4 m, lower than it has been supposed so far ( $5.3 \pm 0.8$  m) [*Little et al.*, 2010]. The 3–4 m R1 offset is similar to a number of offsets that have been measured along other sections of the Wellington fault ( $3 \pm 0.5$  m;  $4 \pm 1$  m; 3.1 m) [*Langridge et al.*, 2005, 2007].

## 6.2. Fault Slip Versus Alluvial History at Te Marua

[59] The slip increments that separate the successive cumulative offsets are 2.9, 4.7, 10.4, 5.2, 2.8, and 5.0 m (Figure 13c). Exact uncertainties on these slip increments are not easy to determine but values of  $\sim 2$  m form an upper bound. The slip increments fall into three subsets, around  $\sim 3$ ,  $\sim 5$ , and  $\sim 10$  m. If, following prior studies, we take these slip increments to be the sum of one to a few large, quite similar earthquake slips, we infer, either that the most recent large earthquakes on the Wellington fault at Te Marua have produced a coseismic slip at surface that was variable in the range 3–5 m, or that the most recent large earthquakes have all produced a similar coseismic slip at the surface of about 3 m. In the former case, the 3–5 and  $\sim 10$  m increments might result from one and two to three large earthquakes, respectively, whereas, in the later case, the  $\sim 3$ ,  $\sim 5$ , and  $\sim 10$  m increments might result from one, two, and three large earthquakes, respectively. We cannot discriminate these hypotheses and hence keep them both in mind in the following. Whatever it is, there is obviously a gap in the slip record between the  $\sim 7.6$  and the  $\sim 18.0$  m offsets.

[60] The common vision that underlies the use of terraces to derive fault and earthquake slips, especially in New

Zealand, is that the active channel before the lower-tread abandonment laterally erodes the riser right above and hence trims any fault offset that the riser might have sustained [*Knuepfer*, 1987; *Lensen*, 1964; *Suggate*, 1960; *Little et al.*, 2010; *Ninis et al.*, 2013]. The riser displacement is thus presumed to accrue only after the lower-terrace surface has been abandoned [e.g., *Cowgill*, 2007]. This is not what we observe in our data. Figure 11 (red dotted lines) shows that the risers R3, R4, R5, R6a, and R6b have recorded roughly the same cumulative offset than the markers that dissect the upper terrace above them. Therefore, these risers have not been trimmed by their lower channel.

[61] Below we propose a scenario that is consistent with the above observations. The scenario is sketched on Figure S8, where the Hutt River meander migration, terrace formation, and large earthquake history are presented. While the T6b Hutt River channel was active, one or two large earthquakes occurred, that laterally displaced the back risers R6b and R7a and the upper terraces. No large earthquake then occurred in the period of time when the Hutt River meander was migrating westward from T6b to T6a. A new large earthquake occurred when the Hutt River was flowing over T6a. Later on, one or two new large earthquakes broke the fault when the Hutt River was flowing over T5. The subsequent period of time when the Hutt River was flowing over T4 was quiescent. Then again, two to three large earthquakes broke the fault at the time when the Hutt River was flowing over T3. The gap in the slip record between the  $\sim 7.6$  and the  $\sim 18.0$  m offsets might be due to T3 being too narrow where it crosses the fault to show any record (Figure 7). The subsequent period of time when the Hutt River was flowing over T2 was quiescent. Yet, one (and less likely two) large earthquake occurred when the river was just starting migrating further westward and abandoning T2. At that time, the R1 riser was hardly incised and hence could not record any slip. Eventually, one large earthquake occurred after T2 had been fully abandoned and hence when riser R1 was fully formed.

[62] Our work does not provide any age data that would help constraining the above scenario. Though prior workers made significant efforts to date the Te Marua terraces, only a few fairly well-constrained ages are available. In particular, of the 18 OSL dating performed by *Little et al.* [2010], 12 had to be rejected as they yielded ages inconsistent with the stratigraphy (Figure S1). The remaining few data suggest that the T12, T11, T9, and T6a terraces were abandoned at 12–13 ka (three samples),  $11.1 \pm 1.1$  ka (one sample),  $9.6 \pm 0.8$  ka (one sample), and  $4.5 \pm 0.4$  ka (one sample), respectively [*Little et al.*, 2010]. As it is likely that the formation and abandonment of the terraces are diachronous in the cross-valley direction [e.g., *Hancock and Anderson*, 2002; *Pazzaglia*, 2013], more data would be needed to validate these ages. Several charcoal samples were also dated in the three youngest terraces, and though the ages showed a large variability in each terrace (see synthesis in *Langridge et al.* [2011]), it is proposed that T3, T2, and T1 were abandoned around  $1725 \pm 35$  yr BP, 310 yr BP, and less than 250 yr BP, respectively.

[63] From these available age data, we infer that: (1) the two most recent large events might have occurred since

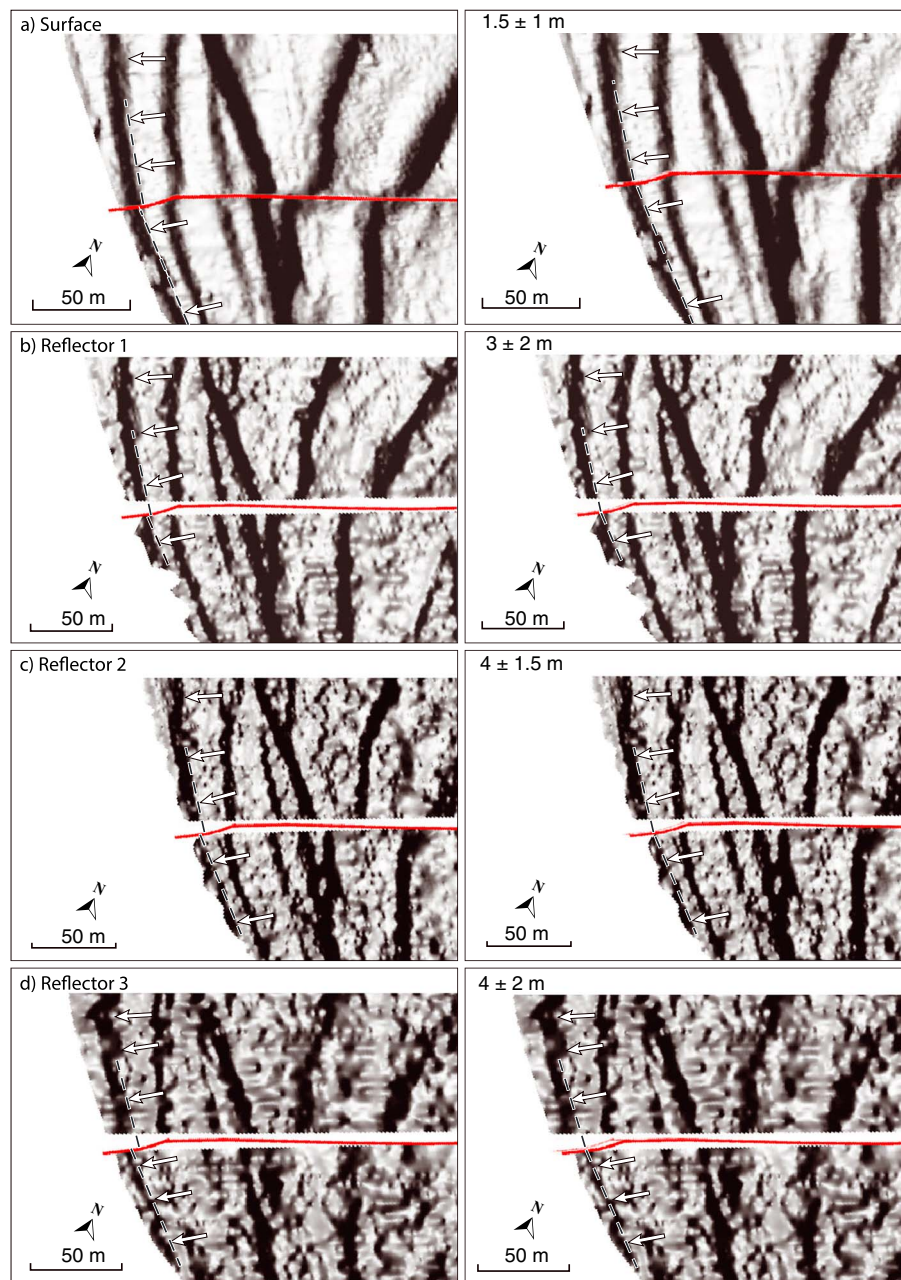


**Figure 14.** Focus on the smallest slip measurement across riser R1. The measurement is shown performed at (a) the ground surface, (b) for Refl1, (c) for Refl2, and (d) for Refl3, in all cases on the hillshade representation of the topographic data, illuminated from the NE, and built at 1 m resolution. The left panel shows the present topography, whereas the right panel shows the topography after the back slip reconstruction of R1 has been done. The two offset sections of riser R1 are highlighted with white dotted lines. The amount of lateral offset necessary for each reconstruction (i.e., adjustment of the two white dotted lines across the fault trace) is indicated along with its uncertainties (from Table S1 in supporting information).

~310 cal yr BP. As there has been no large earthquake on the Wellington fault since the arrival of Europeans in Wellington in A.D. 1840, the two most recent large events would have occurred between A.D. 1640 and 1840, as previously inferred for a single event [Langridge *et al.*, 2011]; (2) two to three large earthquakes occurred little before ~1700 yr BP; (3) five to eight large earthquakes occurred in the last ~4.5 ka; and (4) 7 to 11 large earthquakes might have occurred since the abandonment of T7b, at most over

the last ~10 ka. These inferences are consistent with prior paleoseismological findings (see section 2).

### 6.3. Implications for Fault Slip Recovery in Paleoseismology

[64] Our work sheds a new light on the way paleoseismological fault slips might be recovered.

[65] First, we confirmed the generally accepted issue that using a large, high-resolution DEM of the ground surface is

mandatory to properly recover the morphological imprints of past fault slips. The DEM coverage must be large enough to constrain the overall geometry of the displaced markers, without or with limited bias from near-fault trace complexities. The DEM resolution must also be high enough to permit identifying and mapping a large number of offset features of various scales and precisely measuring their offsets. One key result that emerges from this approach is that the increase in the number of identified features and hence of offset measurements goes along with a decrease in the number of statistically, robustly constrained offsets. From the 26 distinct offsets that we measured at the ground surface, only two robustly supported offset values are retained, while only two more values are suggested as fairly well supported (see section 5.2). This result arises from the variable uncertainties on the measurements which, when taken into account, dramatically decrease the number of offset values that are well discriminated from one another. This result might call to treat with caution the fault offsets that have been inferred in prior works from a limited number of measurements at the ground surface. It is noteworthy that the few recent studies that could measure larger amounts of fault offsets at sites where previous studies had reported a more limited number of measurements provide significantly different offset values [Zielke *et al.*, 2010; Schlagenhauf *et al.*, 2011; Klinger *et al.*, 2011; Beaupretre *et al.*, 2012; Rockwell and Klinger, 2013; Benedetti *et al.*, 2013].

[66] Second, our work shows that the use of GPR data at Te Marua provides a novel opportunity to measure each offset several times, at different depths. This densification of the measurements allows to even better constrain the preserved fault offsets and to more tightly define their uncertainties. The subsurface measurements are found to be systematically slightly different from those measured at the ground surface on the same markers. This systematic difference might arise from the surface record being slightly altered compared with the buried and hence better preserved subsurface record. Although this situation is partly site dependent, we suggest that it might be the case in many other sites worldwide where the ground surface sustains significant erosion, deposition or human activity.

[67] Along with our earlier work on the Hope fault [Beaupretre *et al.*, 2012], the present study thus suggests that pseudo-3D GPR is a powerful paleoseismological tool that could be used in complement to surface observation to recover the past fault slips. In the Te Marua case, the GPR data additionally allow documenting the 3D stratigraphic architecture of the alluvial terraces, an information that was previously unknown. At Terako (Hope fault), the GPR data revealed offset features that were completely invisible at the ground surface, and thus, out of reach of conventional paleoseismological tools. The GPR data also revealed large, and hence old offsets that had not been preserved at the current ground surface, and hence that could not have been studied either with the classical paleoseismological tools. These results suggest that pseudo-3D GPR investigation should be carried out at most paleoseismological sites (where material nature permits it), in complement to other, more classical approaches. In doing so, we may expect that GPR data contribute, not only to identify and measure the fault slips, but also to precisely locate the subsurface features which need to be sampled for dating purposes.

## 7. Conclusions

[68] Our objective was to examine whether, in a specific case where a number of fault offsets have already been carefully measured in the current morphology, the deep subsurface ( $> \sim 2$  m) might still contain additional information that could be useful to further document the past earthquake slips on the fault. We addressed this question at Te Marua (Wellington fault, New Zealand), an extensively studied paleoseismic site with 11 well-preserved, dextrally displaced, alluvial terraces. We investigated the Te Marua site using pseudo-3D GPR combined with a high-resolution GPS-DEM of the site. The GPS DEM allowed us examining the current Te Marua landforms in great details, whereas the GPR data imaged the architecture of the subsurface at high resolution, down to 5–7 m depth.

[69] We found that the GPR data do provide several pieces of information that complement the observations at the ground surface.

[70] First, the GPR data reveal the 3D stratigraphic architecture of the alluvial terraces, which was unknown so far. Each of the T1–T7 Te Marua terrace is found to be a strath terrace that was carved into the graywacke bedrock. Each strath surface is overlain by 3–5 m of horizontally bedded gravel sheets that form a package of layered GPR reflections among which two shallow (1–3 m depth) reflections are especially pronounced.

[71] Second, thanks to the multilayered architecture of the alluvial terraces, the GPR data image the terrace risers and stream channels at different depths. Most of the fault offsets across the various markers can thus be measured up to three to four times, and this densification of the offset measurements allows tightening the fault-offset values and their uncertainties.

[72] Third, as GPR data permit measuring the fault offsets in the principal stratigraphic horizons of the terraces, the possible variability of the offset preservation from the base to the top of the terraces can be examined. Most displacements measured in the subsurface horizons are found to be larger by 1–1.5 m than those measured at the current ground surface, thereby suggesting that lateral offsets in the landforms might be less well preserved than the offsets buried in the subsurface, likely due to subsequent erosion/deposition at the ground surface. In some cases, slip records recovered from surface data only might thus not reveal exactly the actual fault slips.

[73] The present study therefore confirms that pseudo-3D GPR provides an additional paleoseismological tool to complement surface investigations, even when more established techniques like paleoseismic trenching are available. GPR paleoseismology may be particularly useful in places where fault-offset markers are few and/or have been significantly weathered at the ground surface.

[74] Taken together, the surface and subsurface observations show that the Te Marua terraces have recorded six cumulative lateral fault slips, of  $\sim 2.9$ ,  $\sim 7.6$ ,  $\sim 18.0$ ,  $\sim 23.2$ ,  $\sim 26.0$ , and  $\sim 31.0$  m (each  $\pm \sim 2$  m). More broadly, our results suggest that the largest earthquakes on the Wellington fault at Te Marua might produce a coseismic slip in the range 3–5 m near the surface, in the lower range of the coseismic slip estimates provided so far ( $5.0 \pm 0.2$ , Little *et al.*, 2010). Whereas finding a smaller slip per event might slightly reduce the range of magnitudes to be expected for the forthcoming large events on the southern Wellington fault, we ignore what

implications this finding might have on the recurrence times of those large earthquakes. Studies dedicated to densely date the Te Marua terraces are clearly needed to address this question.

[75] **Acknowledgments.** This work has been funded by the French National Research Agency (ANR Project CENTURISK Risknat09\_456076) and has been carried out in the framework of a collaboration between French scientific laboratories, the Geological and Nuclear Science (GNS) of New Zealand, and the University of Canterbury, New Zealand. We are thankful to Wooster for giving us access to their Te Marua field. We are also thankful to David Caterina, Pascale Sénéchal, and Angélique Zajac for helping us during acquisitions on the field. We greatly thank Rob Langridge for introducing us to the Te Marua site and for the fruitful discussions that we had. We thank Y. Gaudemer for his help on fault-offset statistical analysis. We are grateful to O. Zielke and J. Hollingsworth for their thorough and constructive comments on a preliminary draft, which greatly helped improving the manuscript. We are also very grateful to O. Zielke and an anonymous reviewer for their thorough and detailed comments that helped us improving furthermore our paper.

## References

- Annan, A. P. (2005), GPR methods for hydrogeological studies, in *Hydrogeophysics*, edited by Y. Rubin and S. S. Hubbard, vol. 50, pp. 185–213, Springer, Netherlands.
- Annan, A. P. (2009), Electromagnetic principles of ground penetrating radar, in *Ground Penetrating Radar: Theory and Applications*, edited by H. M. Jol, p. 176, Elsevier Science Ltd., Oxford, U.K.
- Barnes, P. M., B. M. de Lépinay, J.-Y. Collot, J. Delteil, and J.-C. Audru (1998), Strain partitioning in the transition area between oblique subduction and continental collision, Hikurangi margin, New Zealand, *Tectonics*, *17*(4), 534–557, doi:10.1029/98TC00974.
- Beanland, S., and J. Haines (1998), The kinematics of active deformation in the North Island, New Zealand, determined from geological strain rates, *N. Z. J. Geol. Geophys.*, *41*, 311–324.
- Beaupretre, S., et al. (2012), Finding the buried record of past earthquakes with GPR-based palaeoseismology: a case study on the Hope fault, New Zealand, *Geophys. J. Int.*, *189*(1), 73–100, doi:10.1111/j.1365-246X.2012.05366.x.
- Begg, J. G., and C. Mazengarb (1996), Geology of the Wellington area, Geol. Map 22, scale 1:50,000, Inst. of Geol. and Nucl. Sci., Lower Hutt, New Zealand.
- Benedetti L., I. Manighetti, Y. Gaudemer, R. Finkel, J. Malavieille, K. Pou, M. Arnold, G. Aumaitre, D. Bourles and K. Keddadouche (2013), More than 30 large earthquakes broke the Fucino faults (Central Italy) in synchrony in the last 12 ka, as revealed from in situ <sup>36</sup>Cl exposure dating, *J. Geophys. Res. Solid Earth*, doi:10.1002/jgrb.50299, in press.
- Berryman, K. R. (1990), Late Quaternary movement on the Wellington Fault in the Upper Hutt area, New Zealand, *N. Z. J. Geol. Geophys.*, *33*, 257–270.
- Berryman, K. R., R. Van Dissen, and V. Mouslopoulou (2002), Recent rupture of the Tararua section of the Wellington fault and relationships to other fault sections and rupture segments, EQC Res. Rep. 97/248, Inst. of Geol. and Nucl. Sci., Lower Hutt, New Zealand.
- Bristow, C. S., and H. H. M. Jol, eds, (2003), *Ground Penetrating Radar (GPR) in Sediments*, Geological Society, London, Special Publications 2003, vol. 211, p. 1–7, 10.1144/GSL.SP.2001.211.01.01
- Bucher, W. H. (1932), “Strath” as a geomorphic term, *Science*, *75*, 130–131.
- Bull, W. B. (1979), Threshold of critical power in streams, *Geol. Soc. Am. Bull.*, *90*(5), 453–464.
- Bull, W. B. (1990), Stream-terrace genesis: implications for soil development, *Geomorphology*, *3*, 351–367.
- Burbank, D., and R. Anderson (2001), *Tectonic Geomorphology*, 273 pp., Blackwell Science, Mass.
- Campbell, M. R. (1929), The river system, a study in the use of technical geographic terms, *J. Geophys. Res.*, *28*, 123–128.
- Carpentier, S. F. A., A. G. Green, R. Langridge, S. Boschetti, J. Doetsch, A. N. Abächerli, H. Horstmeier, and M. Finnemore (2012), Flower structures and Riedel shears at a step over zone along the Alpine Fault (New Zealand) inferred from 2-D and 3-D GPR images, *J. Geophys. Res.*, *117*, B02406, doi:10.1029/2011JB008749.
- Cassidy, N. (2009), Ground Penetrating Radar data processing, modelling, and analysis, in *Ground Penetrating Radar: Theory and Applications*, edited by H. M. Jol, 176 p., Elsevier Science Ltd., Oxford, U.K.
- Cohen, J. K., and Stockwell Jr, J. W. (1999), CWP/SU: Seismic Unix Release 33: a free package for seismic research and processing, Center for Wave Phenomena, Colorado School of Mines.
- Cowgill, E. (2007), Impact of riser reconstructions on estimation of secular variation in rates of strike-slip faulting: Revisiting the Cherchen River site along the Altyn Tagh fault, NW China, *Earth Planet. Sci. Lett.*, *254*, 239–255, doi:10.1016/j.epsl.2006.09.015.
- Deparis, J., and S. Garambois (2009), On the use of dispersive APVO GPR curves for thin-bed properties estimation: Theory and application to fracture characterization, *Geophysics*, *74*(1), J1–J12.
- Fisher, S. C., R. R. Stewart, and H. M. Jol, (1994), Processing Ground Penetrating Radar Data, In *Proceedings of the 5th Int. Conf. on G.P.R.*, pp. 661–675, Kitchener, Ontario, Canada.
- Garambois, S., P. Sénéchal, and H. Perroud (2002), On the use of combined geophysical methods to assess water content and water conductivity of near-surface formations, *J. Hydrol.*, *259*(1), 32–48.
- Gaudemer, Y., P. Tapponnier, B. Meyer, G. Peltzer, S. Guo, Z. Chen, H. Dai, and I. Cifuentes (1995), Partitioning of Crustal Slip Between Linked, Active Faults in The Eastern Qilian Shan, And Evidence For a Major Seismic Gap, the Tianzhu Gap, on the Western Haiyuan Fault, Gansu (China), *Geophys. J. Int.*, *120*(3), 599–645.
- Gilbert, G. K. (1877), Report on the geology of the Henry Mountains [Utah]: Publication of the Powell Survey, U.S. Government Printing Office, Washington D.C., 160 p.
- Gold, R. D., E. Cowgill, J. R. Arrowsmith, X. Chen, W. D. Sharp, K. M. Cooper, and X. F. Wang (2011), Faulted terrace risers place new constraints on the late Quaternary slip rate for the central Altyn Tagh fault, northwest Tibet, *Geol. Soc. Am. Bull.*, *123*(5–6), 958–978.
- Grapes, R. H. (1993), Letters to the editor: Terrace correlation, dextral displacements, and slip rate along the Wellington Fault, North Island, New Zealand, *N. Z. J. Geol. Geophys.*, *36*, 131–135.
- Grasmueck, M., R. Weger, and H. Horstmeier (2005), Full-resolution 3D GPR imaging, *Geophysics*, *70*(1), K12–K19.
- Gross, R., K. Holliger, A. Green, and J. Begg (2000), 3D ground penetrating radar applied to paleoseismology: examples from the Wellington Fault, New Zealand, In *Proceedings of the 8th International Conference G.P.R., Gold Coast, Australia* (pp. 478–481).
- Gross, R., A. Green, K. Holliger, H. Horstmeier, and J. Baldwin (2002), Shallow geometry and displacements on the San Andreas Fault near Point Arena based on trenching and 3-D georadar surveying, *Geophys. Res. Lett.*, *29*(20), 1973, doi:10.1029/2002GL015534.
- Gross, R., A. Green, H. Horstmeier, and K. Holliger (2003), 3-D georadar images of an active fault: Efficient data acquisition, processing and interpretation strategies, *Subsurface Sens. Technol. Appl.*, *4*, 19–40, doi:10.1023/A:1023059329899.
- Gross, R., A. G. Green, H. Horstmeier, and J. H. Begg (2004), Location and geometry of the Wellington Fault (New Zealand) defined by detailed three-dimensional georadar data, *J. Geophys. Res.*, *109*, B05401, doi:10.1029/2003JB002615.
- Hancock, G. S., and R. S. Anderson (2002), Numerical modeling of fluvial strath-terrace formation in response to oscillating climate, *Geol. Soc. Am. Bull.*, *114*(9), 1131–1142.
- Klinger, Y., M. Etchebes, P. Tapponnier, and C. Narteau (2011), Characteristic slip for five great earthquakes along the Fuyun fault in China, *Nat. Geosci.*, *4*(6), 389–392.
- Kneupper, P. L. K. (1987), Changes in Holocene slip rates in strike-slip environments, U.S. Geol. Surv. Open File Rep. 249–261.
- Langridge, R. M., K. R. Berryman, and R. J. Van Dissen (2005), Defining the geometric segmentation and Holocene slip rate of the Wellington Fault, New Zealand: the Pahiatua section, *N. Z. J. Geol. Geophys.*, *48*, 591–607.
- Langridge, R. M., K. R. Berryman, and R. J. Van Dissen (2007), Late Holocene paleoseismicity of the Pahiatua section of the Wellington Fault, New Zealand, *N. Z. J. Geol. Geophys.*, *50*, 205–226.
- Langridge, R. M., R. Van Dissen, P. Villamor, and T. Little (2009), It’s our fault—Wellington fault paleoearthquake investigations: Final report, Consult. Rep. 2008/344, GNS Sci., Lower Hutt, New Zealand.
- Langridge, R., R. Van Dissen, D. Rhoades, P. Villamor, T. Little, N. Litchfield, K. Clark, and D. Clark (2011), Five Thousand Years of Surface Ruptures on the Wellington Fault, New Zealand: Implications for Recurrence and Fault Segmentation, *Bull. Seismol. Soc. Am.*, *101*(5), 2088–2107, doi:10.1785/0120100340.
- Lensen, G. J. (1958), The Wellington Fault from Cook Strait to Manawatu Gorge, *N. Z. J. Geol. Geophys.*, *1*, 178–196.
- Lensen, G. J. (1964), The general case of progressive displacement of flights of degradational terraces, *N. Z. J. Geol. Geophys.*, *7*, 864–870.
- Little, T. A., R. J. Van Dissen, U. Rieser, E. G. C. Smith, and R. M. Langridge (2010), Coseismic strike slip at a point during the last four earthquakes on the Wellington fault near Wellington, New Zealand, *J. Geophys. Res.*, *115*, B05403, doi:10.1029/2009JB006589.
- Liu, J., Y. Klinger, K. Sieh, and C. M. Rubin (2004), Six similar sequential ruptures of the San Andreas fault, Carrizo Plain, *Calif. Geol.*, *32*, 649–652.
- Lowell, T. V. (1995), The application of radiocarbon age estimates to the dating of glacial sequences: an example from the Miami sublobe, Ohio, U.S.A., *Quat. Sci. Rev.*, *14*, 85–99.
- Mackin, J. H. (1937), Erosional history of the Big Horn Basin, Wyoming, *Geol. Soc. Am. Bull.*, *48*, 813–893.

- Manighetti, I., M. Campillo, S. Bouley, and F. Cotton (2007), Earthquake scaling, fault segmentation, and structural maturity, *Earth Planet. Sci. Lett.*, 253(3), 429–438.
- McCalpin, J. P. (Ed.) (2009), *Paleoseismology*, vol. 95, 613 pp., International Geophysics, Academic Press.
- McClymont, A. F., A. G. Green, R. Streich, H. Horstmeyer, J. Tronicke, D. C. Nobes, J. R. Pettinga, J. K. Campbell, and R. M. Langridge (2008a), Visualization of active faults using geometric attributes of 3D GPR data: An example from the Alpine Fault Zone, New Zealand, *Geophysics*, 73(2), B11–B23.
- McClymont, A. F., A. G. Green, P. Villamor, H. Horstmeyer, C. Grass, and D. C. Nobes (2008b), Characterization of the shallow structures of active fault zones using 3-D ground-penetrating radar data, *J. Geophys. Res.*, 113, B10315, doi:10.1029/2007JB005402.
- McClymont, A. F., A. G. Green, A. Kaiser, H. Horstmeyer, and R. M. Langridge (2010), Shallow fault segmentation of the Alpine fault zone, New Zealand revealed from 2- and 3-D GPR surveying, *J. App. Geophys.*, 70(4), 343–354, doi:10.1016/j.jappgeo.2009.08.003.
- McGill, S. F., and K. Sieh (1991), Surficial Offsets on the Central and Eastern Garlock Fault associated with prehistoric earthquakes, *J. Geophys. Res.*, 96(B13), 21,597–21,621, doi:10.1029/91JB02030.
- Merritts, D., and T. Hesterberg (1994), Stream Networks and Long-Term Surface Uplift in the New Madrid Seismic Zone, *Science*, 265(5175), 1081–1084.
- Mouslopoulou, V., A. Nicol, T. A. Little, and J. J. Walsh (2007), Displacement transfer between intersecting regional strike-slip and extensional fault systems, *J. Struct. Geol.*, 29(1), 100–116, doi:10.1016/j.jsg.2006.08.002.
- Neal, A. (2004), Ground-penetrating radar and its use in sedimentology: principles, problems and progress, *Earth-Sci. Rev.*, 66, 261–330, doi:10.1016/j.earscirev.2004.01.004.
- Nicol, A., C. Mazengarb, F. Chanier, G. Rait, C. Uruski, and L. Wallace (2007), Tectonic evolution of the active Hikurangi subduction margin, New Zealand, since the Oligocene, *Tectonics*, 26, TC4002, doi:10.1029/2006TC002090.
- Ninis, D., T. A. Little, R. J. Van Dissen, N. J. Litchfield, E. G. C. Smith, N. Wang, U. Rieser, and C. M. Henderson (2013), Slip Rate on the Wellington Fault, New Zealand, during the Late Quaternary: Evidence for Variable Slip during the Holocene, *Bull. Seismol. Soc. Am.*, 103(1), 559–579, doi:10.1785/0120120162.
- Ozawa, S., T. Nishimura, H. Suito, T. Kobayashi, M. Tobita, and T. Imakiire (2011), Coseismic and postseismic slip of the 2011 magnitude-9 Tohoku-Oki earthquake, *Nature*, 475(7356), 373–376.
- Pazzaglia, F. J., (2013), Fluvial terraces, in *Treatise of Geomorphology*, pp. 379–412, vol. 9, Fluvial Landforms, edited by J. F. Shroder, Elsevier.
- Pondard, N., and P. M. Barnes (2010), Structure and paleoearthquake records of active submarine faults, Cook Strait, New Zealand: Implications for fault interactions, stress loading, and seismic hazard, *J. Geophys. Res.*, 115, B12320, doi:10.1029/2010JB007781.
- Rockwell, T. K., and Y. Klinger (2013), Surface rupture and slip distribution of the 1940 Imperial Valley earthquake, Imperial Fault, Southern California: Implications for rupture segmentation and dynamics, *Bull. Seismol. Soc. Am.*, 103(2A), 629–640.
- Schlagenhauf, A., I. Manighetti, L. Benedetti, Y. Gaudemer, R. Finkel, J. Malavieille, and K. Pou (2011), Earthquake supercycles in Central Italy, inferred from 36Cl exposure dating, *Earth Planet. Sci. Lett.*, 307(3), 487–500.
- Seidl, M. A., and W. E. Dietrich (1993), The problem of channel erosion into bedrock, *Catena Suppl.*, 23, 101–101.
- Stolt, R. H. (1978), Migration by Fourier transform, *Geophysics*, 43(1), 23–48.
- Suggate, R. P. (1960), The interpretation of progressive fault displacement of flights of terraces, *N. Z. J. Geol. Geophys.*, 3, 364–374.
- Taner, M. T. (2001), Seismic attributes, *CSEG recorder*, 26(7), 48–56.
- Tapponnier, P., F. J. Ryerson, J. van der Woerd, A.-S. Mériaux, and C. Lasserre (2001), Long-term slip rates and characteristic slip: Keys to active fault behaviour and earthquake hazard, *C. R. Acad. Sci., Ser. II*, 333(9), 483–494.
- Taylor, J. R. (1997), *An Introduction to Error Analysis: The Study of Uncertainties in Physical Measurements*, University Science Book, Sausalito, Calif.
- Tronicke, J., P. Vilamor, and A. G. Green (2004), Estimating vertical displacement within the Ngakuru Graben, New Zealand, using 2-D and 3-D georadar, in *Proceedings of the Tenth International Conference on Ground Penetrating Radar*, 21–24 June, Delft, The Netherlands.
- Van Dissen, R. J., and K. R. Berryman (1996), Surface rupture earthquakes over the last 1000 years in the Wellington region, New Zealand, and implications for ground shaking hazard, *J. Geophys. Res.*, 101(B3), 5999–6019.
- Van Dissen, R. J., K. Berryman, J. R. Pettinga, and N. L. Hill (1992), Paleoseismicity of the Wellington–Hutt Valley segment of the Wellington fault, North Island, New Zealand, *N. Z. J. Geol. Geophys.*, 35, 165–176.
- von Borstel, O. I., and M. Ingham (2004), Imaging the Wairarapa Fault at Tauwharenikau using magnetotelluric sounding, *N. Z. J. Geol. Geophys.*, 47, 281–286.
- Wegmann, K. W., and F. J. Pazzaglia (2002), Holocene strath terraces, climate change, and active tectonics: The Clearwater River basin, Olympic Peninsula, Washington State, *Geol. Soc. Am. Bull.*, 114(6), 731–744.
- Zielke, O., J. R. Arrowsmith, L. G. Ludwig, and S. O. Akçiz (2010), Slip in the 1857 and Earlier Large Earthquakes Along the Carrizo Plain, San Andreas Fault, *Science*, 327(5969), 1119–1122.